NOVEMBER 1993

WRL Research Report 93/7

Fluoroelastomer Pressure Pad Design for Microelectronic Applications

Alberto Makino
William R. Hamburgen
John S. Fitch

digital **Western Research Laboratory** 250 University Avenue Palo Alto, California 94301 USA

The Western Research Laboratory (WRL) is a computer systems research group that was founded by Digital Equipment Corporation in 1982. Our focus is computer science research relevant to the design and application of high performance scientific computers. We test our ideas by designing, building, and using real systems. The systems we build are research prototypes; they are not intended to become products.

There two other research laboratories located in Palo Alto, the Network Systems Laboratory (NSL) and the Systems Research Center (SRC). Other Digital research groups are located in Paris (PRL) and in Cambridge, Massachusetts (CRL).

Our research is directed towards mainstream high-performance computer systems. Our prototypes are intended to foreshadow the future computing environments used by many Digital customers. The long-term goal of WRL is to aid and accelerate the development of high-performance uni- and multi-processors. The research projects within WRL will address various aspects of high-performance computing.

We believe that significant advances in computer systems do not come from any single technological advance. Technologies, both hardware and software, do not all advance at the same pace. System design is the art of composing systems which use each level of technology in an appropriate balance. A major advance in overall system performance will require reexamination of all aspects of the system.

We do work in the design, fabrication and packaging of hardware; language processing and scaling issues in system software design; and the exploration of new applications areas that are opening up with the advent of higher performance systems. Researchers at WRL cooperate closely and move freely among the various levels of system design. This allows us to explore a wide range of tradeoffs to meet system goals.

We publish the results of our work in a variety of journals, conferences, research reports, and technical notes. This document is a research report. Research reports are normally accounts of completed research and may include material from earlier technical notes. We use technical notes for rapid distribution of technical material; usually this represents research in progress.

Research reports and technical notes may be ordered from us. You may mail your order to:

Technical Report Distribution
DEC Western Research Laboratory, WRL-2
250 University Avenue
Palo Alto, California 94301 USA

Reports and notes may also be ordered by electronic mail. Use one of the following addresses:

Digital E-net:	`DECWRL::WRL-TECHREPORTS`
Internet:	`WRL-Techreports@decwrl.dec.com`
UUCP:	`decwrl!wrl-techreports`

To obtain more details on ordering by electronic mail, send a message to one of these addresses with the word ‘‘`help`’’ in the Subject line; you will receive detailed instructions.

Fluoroelastomer Pressure Pad Design for Microelectronic Applications

Alberto Makino
William R. Hamburgen
John S. Fitch

November 1993

digital **Western Research Laboratory** 250 University Avenue Palo Alto, California 94301 USA

Abstract

The elastic properties of gum rubber and fluoroelastomers were studied by a variety of numerical and experimental methods. Results were applied to the design of flat pressure pads for microelectronic applications. The goal was to develop an understanding sufficient that designers could quickly develop acceptable fluoroelastomer pressure pads without further detailed studies. The effort centered on optimizing the performance of a 14 mm square by 0.8 mm thick pad under a fixed normal force. The primary optimization criterion was minimization of the maximum normal contact stresses applied by the pad to a rigid surface.

Judicious perforation of flat pads greatly reduced adverse contact stress gradients. The preferred design used four 1.2 mm holes symmetrically arrayed in a 4 mm square grid centered on the pad. Compared to an unperforated pad, this arrangement yielded a 28% reduction in maximum contact stresses.

Contents

List of Figures

Nomenclature

c_{ij}	: Cauchy deformation tensor
e_{ij}	: Eulerian finite deformation tensor
l_0	: original gage length in a test sample
l_s	: deformed gage length in a test sample
n	: number of experimental data points
p	: arbitrary hydrostatic traction, inflation pressure
r	: radius of curvature in an inflated membrane
t_0	: initial thickness in a test sample
t_s	: thickness in a deformed sample
u_i, u_j	: displacements
$x_{i,A}$	: deformation gradient tensor
C_{ijk}, C_{ij}	: material constants in a series expansion of W
C_{AB}	: Green deformation tensor
E_{AB}	: Lagrangian finite deformation tensor
$F_{i,A}$	: deformation gradient tensor
I_1, I_2, I_3	: invariants of the stretches
W, $W(I_1, I_2, I_3)$	: potential strain energy density function
$\boldsymbol{c}$	: Cauchy deformation tensor
$\boldsymbol{i}_i$	: basis vector of the deformed configuration
$\boldsymbol{n}$	: unit vector associated with the current configuration
$\boldsymbol{x}$	: position vector of a point after a finite deformation
$\boldsymbol{C}$	: Green deformation tensor
$\boldsymbol{I}_A$	: basis vector of the undeformed configuration
$\boldsymbol{N}$	: unit vector associated with the original configuration
$\boldsymbol{X}$	: position vector of a point in the undeformed configuration
α_i	: material constants in Ogden's strain energy function
δ_{ij}, δ_{AB}	: Kroenecker delta
ε	: engineering strain
ε_{ij}	: strains (infinitesimal theory)
θ	: angle subtended by a deformed gage length l_s
λ, λ_i	: stretch ratio
λ_1, λ_2, λ_3	: stretch ratios along three orthogonal directions
$\lambda_{\boldsymbol{n}}$	: stretch ratio along $\boldsymbol{n}$
μ_i	: material constants in Ogden's strain energy function
σ	: membrane stresses
σ_{ij}	: true (Cauchy) stresses
$\Lambda_{\boldsymbol{N}}$	: stretch ratio along $\boldsymbol{N}$

1 Introduction

Flat sheets of rubber are frequently used to transfer a load from one planar surface to another. Such pads serve to reduce local pressure nonuniformities due to point defects (bumps and voids), as well as large scale distortions (warp, bow, waviness). But owing to the incompressibility of rubber, the pressure applied by a pad is not truly uniform, rather it tends to be highest at the center of the pad, decreasing toward the edges. In some microelectronic applications, such as when the pad contacts the active surface of a silicon microcircuit (die), this pressure nonuniformity is of tremendous importance. Rubber pad use in packaging can be temporary or permanent. An

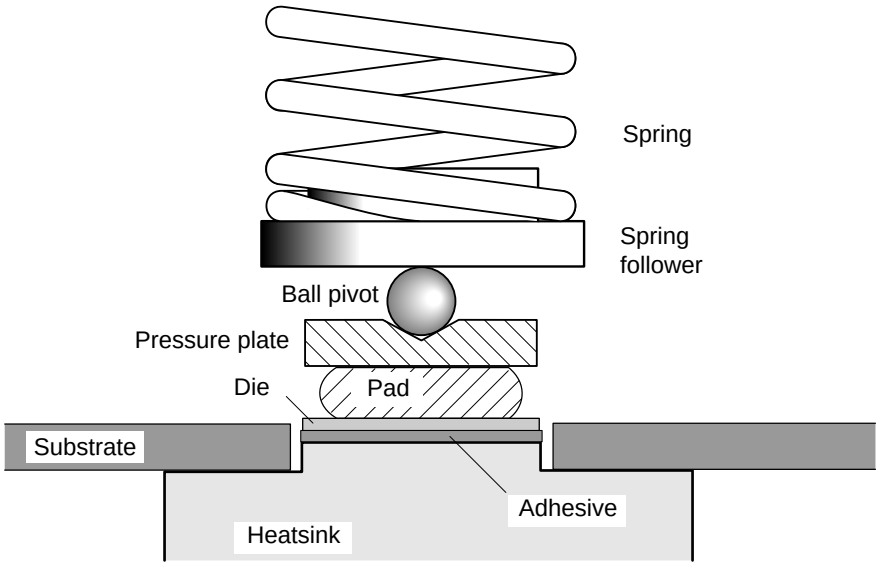

Figure 1: High pressure adhesive die attach process.

example of temporary application occurs when a pad is used to load the adhesive joint during high pressure die attach as shown in Fig.1. The ball pivot keeps the spring force centered on the die, while the rubber pad distributes the force preventing excessive or spatially varying normal contact stresses which may cause die cracking or a nonuniform adhesive thickness distribution [1]. An example of permanent rubber pad application is depicted in Fig.2, where the pad is used in a package to press the die against a heatsink in order to form a pressure contact joint. A similar approach was used for a recent Siemens mainframe computer [2, 3]. In this case, contact stress gradients can lead to corresponding temperature gradients. Figure 2 also shows the importance of understanding pad deformation; if the edges of the pad bulge excessively, bondwire damage may occur. And in both cases, shear tractions applied to the active surface of the die may damage it.

Our laboratory had previously designed such pads by empirical methods, but we wanted to move toward higher pressures for both die attach and pressure contact heat transfer applications. We were concerned about the effects of contact pressure nonuniformity, and decided to embark

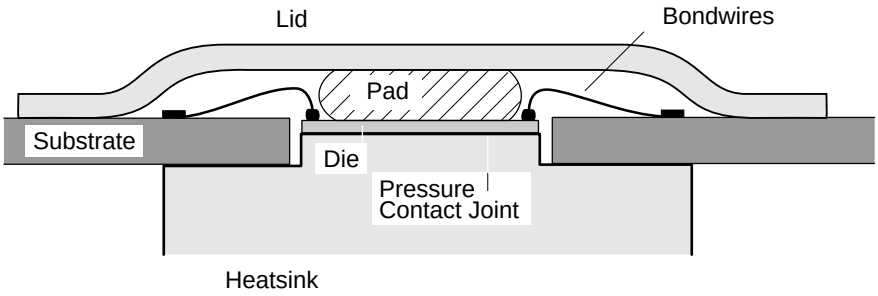

Figure 2: Pressure contact die attach with bondwires.

on the current study.

The force distribution could be modified by using a pad with a 3-D surface profile rather than a flat surface. To reduce costs and lead times, we chose instead to investigate the limitations of shapes stamped from flat stock with low cost punches and steel-rule dies. The Siemens mainframe is also reported to have used perforated pads [4].

We chose two elastomers for our investigation. The first was pure gum rubber, since it is one of the materials whose properties have been most widely reported in the open literature. The second was Viton™ [Du Pont], the fluoroelastomer we had already selected for our end use applications. Viton has excellent chemical resistance and tolerates high temperatures [1] . And while it is much more expensive than conventional compounds, it is a fraction of the cost of fully fluorinated elastomers such as Kalrez™ [Du Pont] and Chemraz™ [Green, Tweed, & Co.]. Viton is also readily available in sheet form in both commercial and MIL-SPEC grades; this proved to be an important distinction. Viton is the commercial name of copolymers of vinylidene fluoride. Several types are available: Viton "A" is a dipolymer of vinylidene fluoride and hexafluoropropylene, Viton "B" and "F" are terpolymers of vinylidene fluoride and combinations of hexafluoropropylene and tetrafluoroethylene [5]. The main difference is their chemical resistance to aggressive substances. The elongation at break is rather low (about 200%) and these compounds are generally stiffer than other rubber-like materials [6].

The goal of our research was to develop a sufficient understanding of the behavior of small Viton pads, so that designers could quickly develop acceptable pressure pad designs without further detailed studies. Both numerical and experimental methods were used. Our work centered on optimizing the behavior a 14 mm square by 0.8 mm thick pad under a fixed normal force. Our primary optimization criteria was minimization of the maximum normal contact stresses applied by the pad surface.

[1] Viton has a long service life even with continuous exposure to 200° C [6]. Typical applications include seals for automotive fuel lines, hydraulic pumps, and flue gas ducts in the power generation industry.

2 Rubber Elasticity

2.1 Finite Elasticity

Rubber and rubber-like materials have the unique capability to withstand large deformations and still be able to fully recover their original dimensions. These materials owe their unusual properties to their molecular structure, which consists of long hydrocarbon chains (often with Cl or Fl substitutions) with a tangled shape and freely rotating links. The hydrocarbon molecules are interlocked in such a way that they form a three dimensional network able to sustain large deformations as chains straighten (Treloar [7] p.12.) Natural and syntehtic rubbers and their derivatives can achieve strains as high as 500%-1000%. In this case "strain" is defined as the percentage change in original length L,

$$\varepsilon = \frac{\Delta L}{L} \times 100 \tag{1}$$

By contrast, most other engineering materials are only able to recover their initial dimensions for strains of at most a few tenths of a percent in uniaxial extension. Within those limits, both rubber and other solids behave elastically, which implies not only the recovery from any imposed deformations but also independence of stresses on previous deformation history.

Engineering materials such as crystalline metals are classified as linear elastic solids whereas

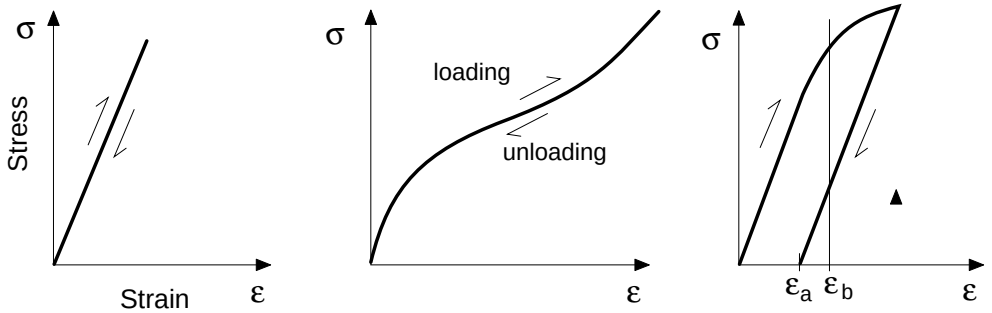

Figure 3: Types of stress-strain responses

rubber-like materials are considered nonlinear elastic solids. The difference is the type of stress-strain behavior as shown in Fig.3. These curves represent the stress-strain response to unixial loading. Figure 3(a) depicts the constant slope response associated with a linear isotropic Hookean material, a class to which most metals belong. Figure 3(b) depicts a behavior typical of rubber-like solids, in which stresses cannot be described as a linear function of strains. In both cases however, the curves during loading and unloading follow the same path; the stress is a unique function of the strain or deformation. Figure 3(c) depicts a third case where the stresses are not a single-valued function of the strains. Stresses during loading and unloading follow

different paths. For a given strain, such as ε_b, there are two possible stress values depending on previous loading history. Also, note that upon unloading to zero stress, the material has acquired a permanent deformation ε_a. This is called inelastic behavior, and is typical of materials when the elastic limit is exceeded.

Deformations in metals loaded within the elastic limits are much less than unity and therefore their behavior can usually be adequately characterized with either a strength of materials approach or its more refined counterpart, the infinitesimal theory of elasticity. Rubber-like materials can exhibit strains that are several orders of magnitude higher, and the same approach cannot be used. The more general finite elasticity theory is needed. All measures, such as strains and stresses, defined for linear isotropic elastic solids have to be recast in the context of a finite deformation theory. It is noted that the infinitesimal theory constitutes a limiting case of the finite deformation theory. Only the fundamental concepts of finite elasticity will be presented here; the interested reader is referred to the many excellent treatises on continuum mechanics and nonlinear elasticity such as Malvern [8], Green and Adkins [9], and Green and Zerna [10].

One of the main differences between the infinitesimal and finite deformation theories is the location at which the stress and strain measures are defined. When deformations are large, the initial and final locations of a particular point such as P in Fig.30 (Appendix A, page 39) may be widely separated. In such cases, motions, strains, and stresses could be defined in two different ways, by referencing them to the initial undeformed configuration or to the current deformed configuration. These are the Lagrangian and Eulerian descriptions [8]. When deformations are small compared to unity, as with metals, this distinction becomes unnecessary and all stress and strain measures collapse into the definitions of the infinitesimal theory. The strain tensor, defined in the infinitesimal theory in terms of displacement gradients as

$$\varepsilon_{ij} = \frac{1}{2}\left(\frac{\partial u_i}{\partial x_j} + \frac{\partial u_j}{\partial x_i}\right) \tag{2}$$

where

ε_{ij} : strains
u_i, u_j : displacements

is replaced in finite elasticity theory by either the Lagrangian or Eulerian finite strain tensor, E_{AB} or e_{ij} (see Appendix A, page 40 and ref.[8]).

Although it is possible to analyze rubber-like materials using finite strains, it is customary to instead use a stretch ratio, λ, defined in the deformed configuration as the ratio of the original and current relative lengths (see Fig.30, page 39, and derivation in page 40),

$$\frac{1}{\lambda} = \frac{dX}{dx} \tag{3}$$

The only differences are the values at zero deformation, where the stretch ratio is $\lambda = 1$ but the Lagrangian and Eulerian strains are $E = e = 0$. A stretch ratio of $\lambda = 2$ in a given direction

indicates that the final dimension is twice the original one. The use of stretch ratios in finite elasticity is a matter of convenience due to the magnitude of the deformations. By contrast, using stretch ratios in the infinitesimal theory would be cumbersome at best. For example, an object with an original length of 1 mm and a final length of 1.001 mm, is much easier to describe using engineering strains ($\varepsilon = 0.1\%$).

Stress measures in finite elasticity theory center around the Cauchy or true stresses which are defined in the deformed configuration [2] .

2.2 Stresses and Constitutive Equations

In most engineering design problems, the load acting on an object is known, or can be assumed to fall within in a certain range. Based on this, the analyst seeks to determine the corresponding effects in the interior of a solid, i.e., investigate stresses and their distribution. Stresses cannot be measured directly and must instead be related to measurable quantities such as strains or stretch ratios through the use of constitutive equations which describe the relationship between stresses and stretch ratios or strains. The independence of stresses on previous deformation history and the reversibility of imposed deformations in elastic materials allows us to prove that constitutive relations for both linear and nonlinear elastic solids can be derived from a strain energy potential function. This argument is very similar to the path independent work done on a particle in a potential field where the forces can be derived from a differentiable potential function [11]. By analogy, if stresses take the place of forces, a differentiable potential function must exist[3] that it is a function only of the deformations. In such cases stresses can be expressed as

$$\sigma_{ij} = \frac{dW(\boldsymbol{e})}{de_{ij}} \tag{4}$$

where

σ_{ij}	: true (Cauchy) stresses
$W(\boldsymbol{e})$	: potential strain energy density function (strain energy per unit volume)
$\boldsymbol{e}$	: any deformation measure (e.g., finite Eulerian strain tensor, stretches)

Any material for which such a potential strain energy function exists is called a Green-elastic or hyperelastic material [8]. In the strictest terms, both linear and nonlinear elastic materials are hyperelastic. In practice however, the term hyperelastic is generally applied only to rubber-like materials. From the mathematical standpoint, there are two ways to apply Eq.4 to obtain a constitutive relation. One is to assume small strains, take a series expansion and consider only

[2]Stresses can also be referenced to the initial undeformed configuration (e.g. the first Piola-Kirchhoff stress tensor). This distinction is necessary due to changes in areas associated with the current and original configurations.

[3]The existence of this function is not always assured.

the linear terms. This leads to the familiar Hooke's law for linear elastic solids. The other is to assume finite strains and construct a suitable strain energy function. The success of any analytical or numerical effort in hyperelastic solids depends closely on the ability of the chosen strain energy function to reproduce the actual material behavior.

In spite of their compliant appearance, most rubbers are incompressible or nearly incompressible solids. This makes them capable of withstanding large hydrostatic tractions without any change in volume and implies that deformations alone cannot describe stress states in the interior of such materials. For example, imagine a rubber ball deep in the ocean. It is subjected to homogeneous external tractions $p = \rho g h$ (ρ: water density, g: acceleration of gravity, h: depth), yet due to its imcompressibility, it has the same dimensions as at sea level. This incompressibilty condition can be expressed as a function of the stretch ratios along three orthogonal directions,

$$\lambda_1 \lambda_2 \lambda_3 = 1 \tag{5}$$

Our focus here will be on homogenous deformations, those in which the deformation gradient $F_{i,A}$ does not depend on the original configuration $\boldsymbol{X}$ (see Appendix A, page 40). Such deformations can be completely characterized with only three stretch ratios along orthogonal directions. The hydrostatic state of the ball in the ocean example is one case. Another is a sample subjected to biaxial extension along two orthogonal axes. Since the unit vectors associated with the original and deformed configurations ($\boldsymbol{N}$ and $\boldsymbol{n}$) do not change orientation in a homogeneous deformation, there is only one stretch measure (see Appendix A, page 41).

In the general case of an isotropic hyperelastic solid, the strain energy density function W must be a symmetrical function of the stretch ratios λ_1, λ_2, and λ_3 (see Rivlin [12] and Treloar [7].) It follows that W can be defined in terms of the three invariants defined as (see Eq.52, Appendix A page 42),

$$\begin{aligned} I_1 &= \lambda_1^2 + \lambda_2^2 + \lambda_3^2 \\ I_2 &= \lambda_1^2\lambda_2^2 + \lambda_2^2\lambda_3^2 + \lambda_1^2\lambda_3^2 \\ I_3 &= \lambda_1^2\lambda_2^2\lambda_3^2 \end{aligned} \tag{6}$$

Thus,

$$W = W(I_1, I_2, I_3) \tag{7}$$

The choice of W can be arbitrary as long as it does not violate any of the principles of continuum mechanics (for example, it must predict zero stress at zero deformation). A suitable general form is a power series of the invariants I_1, I_2, and I_3

$$W(I_1, I_2, I_3) = \sum_{i=0, j=0, k=0}^{\infty} C_{ijk}(I_1 - 3)^i (I_2 - 3)^j (I_3 - 1)^k \tag{8}$$

where

C_{ijk} : material constants

This function is zero at zero deformation as long as C_{000}=0. Also note that by Eq.6, $I_1 = I_2 = 3$ and $I_3 = 1$ for $\lambda_1 = \lambda_2 = \lambda_3 = 1$, and the correct zero stress is predicted by Eq.4.

When the incompressibility condition is introduced, $I_3 = 1$ for any stress state, and the terms affected by it drop from Eq.8 giving

$$W(I_1, I_2) = \sum_{i=0,j=0}^{\infty} C_{ij}(I_1 - 3)^i (I_2 - 3)^j \tag{9}$$

where

C_{ij} : material constants

Again, C_{00}=0 in order to have zero stresses at zero deformation. Generally the first few terms in the series dominate, and we can consider W to be given by the two-term approximation which includes only the linear terms in I_1 and I_2 ($i = 1, j = 0$ and $i = 0, j = 1$),

$$W(I_1, I_2) = C_{10}(I_1 - 3) + C_{01}(I_2 - 3) \tag{10}$$

This is perhaps the form most widely used in rubber elasticity and is known as the Mooney-Rivlin strain energy function, first proposed by Mooney in 1940 [13, 12]. The Mooney-Rivlin form has been found to reproduce the behavior of most natural and synthetic rubbers for moderate deformations ($\lambda \approx 4$). For higher stretch ratios it is less successful, and over the years, a number of other forms for the strain energy function have been proposed in response to the need to characterize a variety of rubber-like materials. Some of these are higher order approximations of Eq.9 and others have been formulated along rather different lines, among them:

- Neo-Hookean form [7]

  $$W = C_{10}(I_1 - 3) \tag{11}$$

  Used only for certain vulcanized rubbers swollen with organic solvents [11]. It gives a poorer fit of experimental data than Mooney-Rivlin's form.

- Rivlin-Saunders form [14]

  $$W = C_{10}(I_1 - 3) + F(I_2 - 3) \tag{12}$$

  where $F(I_2 - 3)$ is a function of I_2. Intended for a general rubber-like material.

- Klosner and Segal [15] cubic form for $F(I_2 - 3)$

  $$W = C_{10}(I_1 - 3) + C_{01}(I_2 - 3) + C_{02}(I_2 - 3)^2 + C_{03}(I_2 - 3)^3 \tag{13}$$

  Tested on natural rubber.

- Ishihara et.al. form [16]

$$W = C_{10}(I_1 - 3) + C_{20}(I_1 - 3)^2 + C_{01}(I_2 - 3) \tag{14}$$

Obtained from non-Gaussian molecular theory considerations. It exhibits poor correlation with uniaxial experimental data on 8% sulfur rubber, Alexander [17].

- Second order deformation form [37]

$$\begin{aligned} W &= C_{10}(I_1 - 3) + C_{01}(I_2 - 3) + C_{20}(I_1 - 3)^2 + \\ &\quad C_{11}(I_1 - 3)(I_2 - 3) + C_{02}(I_2 - 3)^2 \end{aligned} \tag{15}$$

General use. Included in some finite element programs.

- Third order deformation form [18, 19]

$$\begin{aligned} W &= C_{10}(I_1 - 3) + C_{01}(I_2 - 3) + C_{20}(I_1 - 3)^2 + \\ &\quad C_{11}(I_1 - 3)(I_2 - 3) + C_{30}(I_1 - 3)^3 \end{aligned} \tag{16}$$

General use. Included in some finite element programs.

- Yeoh form [20]

$$W = C_{10}(I_1 - 3) + C_{20}(I_1 - 3)^2 + C_{30}(I_1 - 3)^3 \tag{17}$$

Used for carbon black filled rubber vulcanizates in which material constants have a strain-history dependency. Of interest in the automotive tire industry.

- Hart-Smith and Crisp [21, 22] exponential-hyperbolic form,

$$W = C\left(\int e^{k_1(I_1-3)^2} + k_2 ln\frac{I_2}{3}\right) \tag{18}$$

where C, k_1, and k_2 are material constants. Tested on sulfur rubber and cast latex. It does not give good agreement in "Neoprene" (polychloroprene) film under equibiaxial stresses [17].

- Alexander form [17]

$$W = C_1 \int e^{k(I_1-3)^2} dI_1 + C_2 ln\left(\frac{I_2 - 3 + k_1}{k_1}\right) + C_{01}(I_2 - 3) \tag{19}$$

where C_1, C_2, k, and k_1 are material constants. Good agreement on "Neoprene" film.

- Hutchinson, Becker, and Landel form [11]

$$W = C_{10}(I_1 - 3) + C_{20}(I_1 - 3)^2 + B_1(1 - e^{k_1(I_2-3)}) + B_2(1 - e^{k_2(I_2-3)}) \qquad (20)$$

  where B_1, B_2, k_1, and k_2 are material constants. Good agreement for uniaxial and biaxial tests on filled dimethyl siloxane (silicone) rubber.

- Ogden form [23]

$$W = \sum_{i=1}^{\infty} \frac{\mu_i}{\alpha_i}(\lambda_1^{\alpha_i} + \lambda_2^{\alpha_i} + \lambda_3^{\alpha_i} - 3) \qquad (21)$$

  where μ_i, α_i are material constants. Intended for general use.

The Ogden form, Eq.21, is a more general expression than the expansion in Eq.9. It redefines the first two invariants given by Eq.6 as

$$\begin{aligned} I_1 &= (\lambda_1^{\alpha_1} + \lambda_2^{\alpha_1} + \lambda_3^{\alpha_1} - 3) \\ I_2 &= (\lambda_1^{\alpha_2} + \lambda_2^{\alpha_2} + \lambda_3^{\alpha_2} - 3) \end{aligned} \qquad (22)$$

where the exponents are not necessarily integers. When $\alpha_1 = 2$ and $\alpha_2 = -2$, a two-term Ogden formulation is identical to the Mooney-Rivlin strain energy function, Eq.10.

The choice of a strain energy function depends heavily on the material and the stretch ratios to which it will be subjected. For relatively small stretch ratios, say $\lambda < 2$, a linear approximation such as Mooney-Rivlin's is usually quite adequate, but for high stretch ratio ranges, a higher order approximation may be needed.

Once a strain energy function is chosen, one must still determine the material constants C_{ij}, μ_i, etc., and the expression for the stresses. Considering stretch ratios as deformation measures, the stresses are expressed using Eq.4,

$$\sigma_{ij}\delta_{ij} = \lambda_i \frac{\partial W(I_1, I_2)}{\partial \lambda_i} + p \qquad (23)$$

where

δ_{ij}	: Kroenecker delta
p	: hydrostatic pressure
W	: strain energy density function

The additional term, p, can be considered a Lagrange multiplier needed to comply with the incompressibility condition and accounts for any hydrostatic tractions. For example, a uniaxial loading along the first axis can be described by the stretch ratios

$$\lambda_1 = \lambda, \quad \lambda_2 = \lambda_3 = \frac{1}{\sqrt{\lambda}}$$

(since λ_1 is imposed, λ_2 and λ_3 are considered to be equal and obtained from the imcompressibility condition, $\lambda_1\lambda_2\lambda_3 = 1$). If a Mooney-Rivlin material and zero hydrostatic tractions are assumed, then the stresses from Eq.23 are

$$\sigma_{11} = \lambda \left(\frac{\partial W}{\partial I_1}\frac{\partial I_1}{\partial \lambda} + \frac{\partial W}{\partial I_2}\frac{\partial I_2}{\partial \lambda} \right) \tag{24}$$

The invariants are (see Appendix A, page 42),

$$\begin{aligned} I_1 &= \lambda_1^2 + \lambda_2^2 + \lambda_3^2 = \lambda^2 + 2\frac{1}{\lambda} \\ I_2 &= \frac{1}{\lambda_1^2} + \frac{1}{\lambda_2^2} + \frac{1}{\lambda_3^2} = 2\lambda + \frac{1}{\lambda^2} \end{aligned}$$

Substituting the derivatives of the invariants and the Mooney-Rivlin strain energy function into Eq.24 gives,

$$\sigma_{11} = 2\left(\lambda^2 - \frac{1}{\lambda}\right)\left(C_{10} + \frac{1}{\lambda}C_{01}\right) \tag{25}$$

Similar expresssions can be obtained for equibiaxial loadings

$$\lambda_1 = \lambda_2 = \lambda, \quad \lambda_3 = \frac{1}{\lambda^2} \tag{26}$$

$$\sigma_{11} = \sigma_{22} = 2\left(\lambda^2 - \frac{1}{\lambda^4}\right)\left(C_{10} + \lambda^2 C_{01}\right) \tag{27}$$

2.3 Application to Pad Design

The objective of our investigation was to optimize the contact stress distribution in flat Viton pads under a specified normal load. If contact at the pad faces were frictionless, the problem would reduce to one of equibiaxial loading. The pad would expand uniformly, maintaining its original shape, and the contact stresses would be uniform. But in real assemblies the contact is not frictionless. As a bounding case, one can assume perfect friction or adhesion at the pad faces. Since rubber-like materials experience nearly isochoric (volume preserving) deformations, any kinematic constraints that tend to confine the whole or part of the material cause stress gradients. When friction is introduced, Fig.4, the central part of the pad experiences a stiffening response to the lateral confinement. By contrast, portions near the edges are still able to move relatively

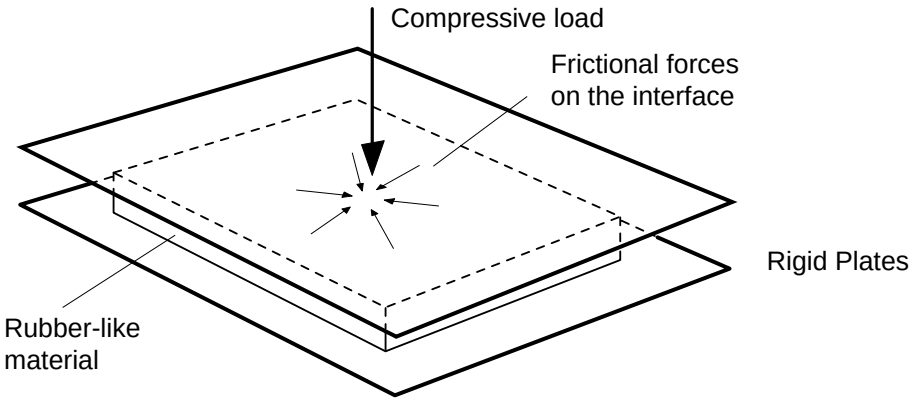

Figure 4: Effect of a finite friction coefficient on material confinement.

freely. This gives rise to substantial radial stress gradients. Placing a hole or perforation in the zone where confinement is expected allows the surrounding material to flow toward the hole's free edge, relieving contact stresses in the vicinity. Our investigation was intended to explore the combined effects of hole placement and size on the contact stress distribution and to reduce its peak value.

In spite of their deceptively simple appearance, the closed form calculation of stresses from the analytical expressions presented so far can be made only in a limited number of cases with simple geometries, boundary conditions, and homogeneous deformations. Experimental methods can be used instead if the time and expense are justified. For example, the contact stress distribution in compressed rubber cylinders has been successfully analyzed by such a method [24]. However, in the vast majority of design cases where direct solutions are not possible the widespread availability of numerical methods such as nonlinear finite element analysis has reduced the need for experimental methods. Commercial codes that include several hyperelastic constitutive models are routinely used in the tire and automotive industries [19]. We chose the same approach to evaluate our pad designs. But first, we needed to determine the material constants for Viton.

3 Material Characterization

In order to use the constitutive models offered by finite element codes, it is necessary to provide values for the various material constants (C_{ij}) defined in the previous section. Unfortunately, there is a wide variation in the properties of synthetic rubbers owing to the large number of compounding variants. The few material constants that have been published in the open literature are for commonly used products such as natural and vulcanized rubbers and pure gum rubber [11]. In practice, it is necessary to characterize each material of interest. This is done by recording the stress-stretch ratio response for simple loading cases and performing a least-

squares fit of the data to an appropriate constitutive relationship. Since different loading modes have slightly different stress-stretch ratio responses, the test loading must be representative of the problem under consideration. It would be incorrect to use material constants obtained, say from an extension test, in a finite element model loaded under pure shear. If the primary loading mode is unknown, then several tests under different loading types are needed and the constitutive model fitted to all experimental points. [4]

The most common homogeneous deformation tests are

- Uniaxial extension
- Equibiaxial extension
- Pure shear

However, the primary loading mode of interest in the design of pressure pads is uniaxial compression. Curiously enough, the superposition principle can be used to show that uniaxial compression of a wide sheet (e.g. a pressure pad) is equivalent to uniform equibiaxial extension. To visualize this, consider the sheet in Fig.5(a), which is subjected to equibiaxial tractions σ, and also subjected to a hydrostatic stress state $-\sigma$. By the superposition principle, the hydrostatic tractions at the edge of the sheet exactly cancel the tractions imposed by the equibiaxial extension. But the faces of the sheet are still subjected to the hydrostatic tractions. The net result is a sheet loaded in uniaxial compression. Hence, we choose an equibiaxial test as the

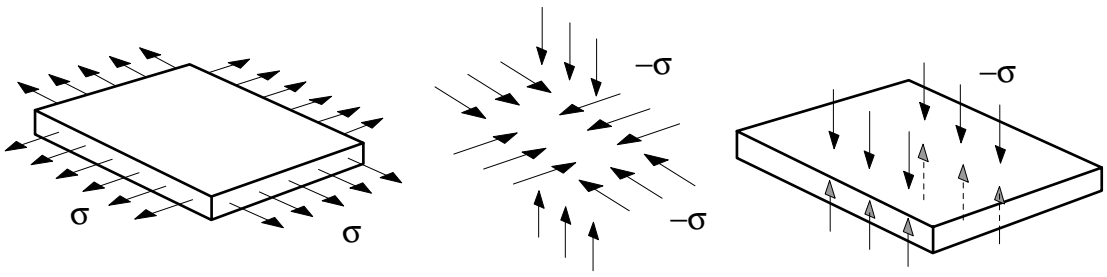

Figure 5: Equivalency of uniform biaxial extension and uniaxial compression

primary means for obtaining material constants for Viton pressure pads.

There are several ways to obtain biaxial extension. One of them involves stretching a sheet of rubber in two orthogonal directions. However, there are a number of problems with this method: the difficulty of maintaining a constant 1:1 load ratio on the two loading directions and the clamping method. Clamping must usually be done with strings in order to avoid nonuniform transmission of the imposed load to the sheet. The load ratio problem can be solved by using

[4] Opinions are still divided on the need for multiple tests. See James et al. [18] for a brief discussion.

dead weights, springs, or a feedback control system with active loading devices. An additional problem is to maintain the load alignment with respect to the deforming sheet (remember the large deformations that rubber can attain). A detailed description of the experimental aspects of this method can be found in refs.[15, 25] [5] .

3.1 Inflation Test

An alternative biaxial extension method, the inflation test, is much simpler to implement. A circular sheet is clamped at its edge and subjected to internal pressurization. When inflated, the sheet acquires a balloon-like shape and as long as its radius of curvature is much greater than its thickness, it can be analyzed as a membrane . If only small areas are considered, say near the pole of the inflated shape, curvature effects can be safely ignored and the sheet can be considered to be under a uniform biaxial load. Historically, this was the first test used to characterize rubber behavior. Treloar and Rivlin and co-workers [26, 27, 28, 14] used it not only to find material constants but also to check the validity of a number of analytical solutions for the membrane inflation problem. Nowadays, the inflation test is used in almost all rubber-like material characterization cases related to numerical solutions and nonlinear finite element analysis [22, 29, 30]. It is also one of the most widely described tests for other applications such as mold filling problems [31]. The objective of an inflation test is to record the stretch ratios as a function of inflation pressure. The stretch ratio vs. pressure data is then processed to calculate material constants.

Three different materials were tested: natural latex, pure gum rubber, and Viton. The 0.8 mm (nominal) thick pure gum and natural latex sheets were used to gauge the validity of our methods by comparing results with published values. Mooney-Rivlin constants for pure gum rubber were previously obtained by Oden and Kubitza [29]. Our 0.8 mm nominal thickness Viton sheets were procured from three different sources[6] in order to evaluate the variability of material constants. One source provided commercial grade sheets while two other vendors provided material conforming to MIL-R-83248 Type 2, class 1 specifications.

Sample preparation consisted of cutting circular sheets 81 mm in diameter from the un-deformed material [7] and marking gage lines as indicated in Fig.6. Gage lengths of $l_0 = 6$ mm were used for Viton and $l_0 = 3$ mm for natural latex and pure gum rubber. Longer gage lengths were more appropriate for Viton samples due to their relatively low ultimate elongation values (approximately 150% per ASTM D 412 [32]). While other investigators recommended using the finest possible gage lines [14], we found this unnecessary since we were able to make

[5]The investigations reported in these references by Treloar and Klosner and Segal were concerned with biaxial loadings with ratios other than 1:1. Such biaxial tests are an alternative to a purely unixial test.

[6]See supplier list in App.B, page 44.

[7]This did not correspond to the diameter of the free area able to deform during inflation, the free area is indicated with dashed lines in Fig.6.

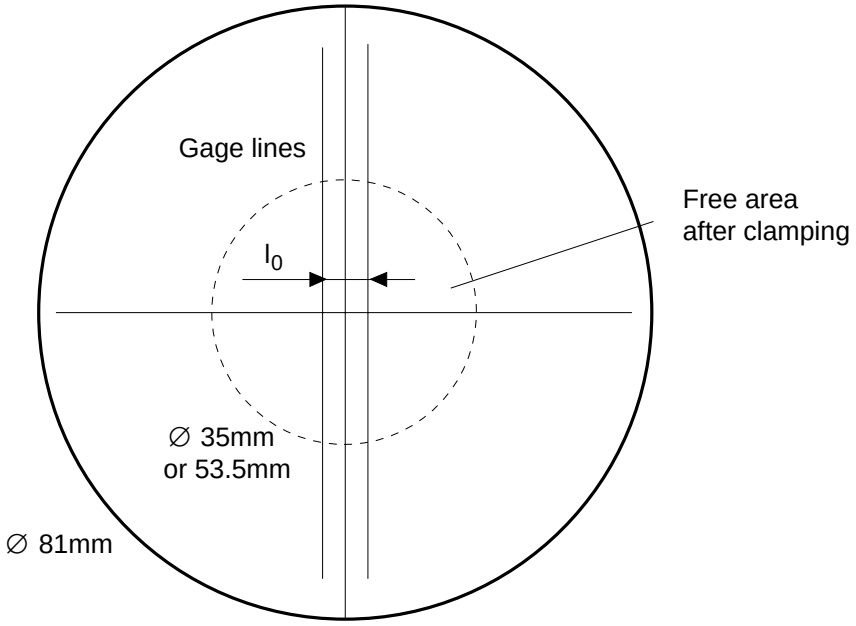

Figure 6: Gage length tracing on a circular sheet

accurate measurements to the edges of the lines. A solvent-based metallic "silver marker" was found to give the best color contrast against the normally dark Viton. A 0.25mm drafting pen with water-based black ink was used to mark both the amber colored natural latex and light brown pure gum rubber. Ink adhesion proved to be very important, especially at large stretch ratios ($\lambda > 4$) when lines tended to lose cohesion and "blur" due to the highly extended state of the material. An optical stage with an attached straight edge was used to accurately mark the gage lines. We also evaluated Nd:YAG laser marking, but found that visible marks damaged the material, particularly the heavily loaded Viton.

The apparatus used to perform the inflation tests consisted of a circular pressure chamber capped by the test sample and sealed with an annular clamp, Fig.7. Dry compressed air was used as the pressurizing fluid. The base and clamps were machined from 6061 aluminum stock. The base included ports for pressure measurements and to admit and vent air. Air inlet control was via a needle valve. Pressure measurements were made with a 0-344 kPa (0-50 psi) pressure transducer for Viton and a precision 0-206 kPa (0-30 psi) Bourdon gage for natural latex and pure gum rubber. Both instruments were calibrated against mercury and water manometers. Both pressure gages could be connected at the same time. A second needle valve was used to deflate the membrane while recording the corresponding stretch ratio response. The entire apparatus was designed to fit on the $x - y$ stage of a Nikon universal measurement microscope.

Two clamp sizes were used for the tests. Natural latex and pure gum rubbers were tested with a clamp allowing for a 35mm diameter free zone. However, due to its low ultimate elongation, Viton required a larger 53.5mm diameter clamp in order to achieve a sufficiently

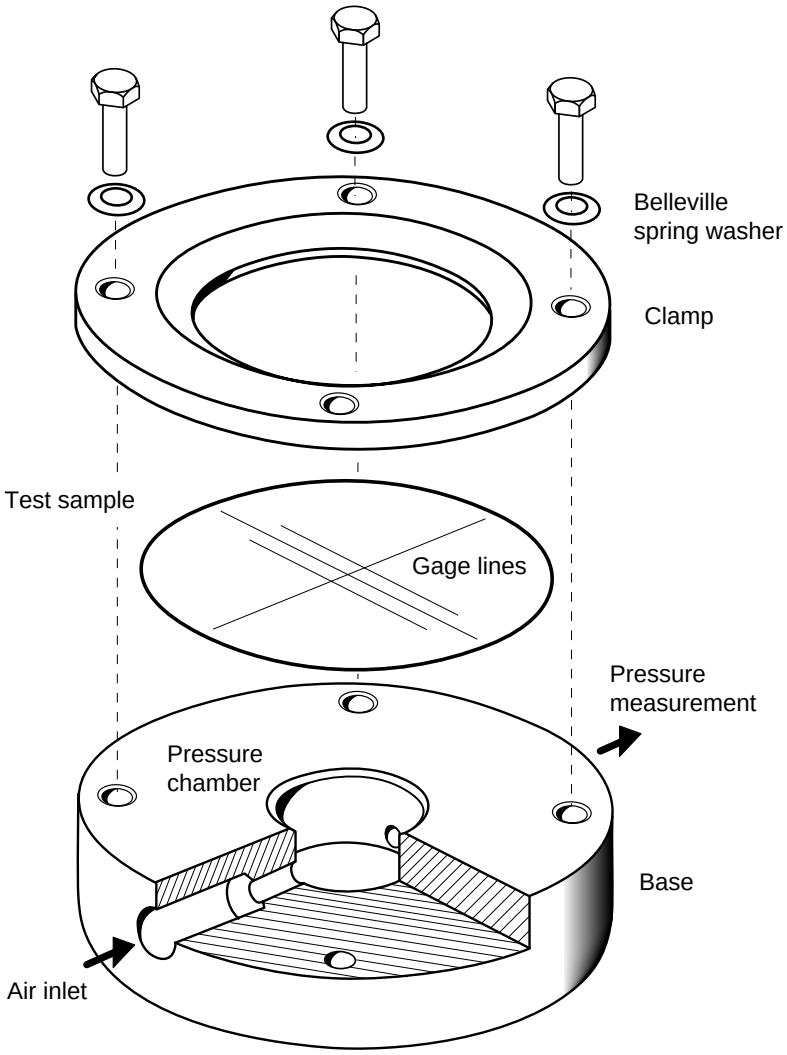

Figure 7: Inflation test apparatus.

large radius of curvature in the inflated shape. Both clamps were machined with a beveled edge as depicted in Fig.7 to allow for free deformation of the inflated sheet. Belleville spring washers under the clamping bolts proved useful in preventing air leaks over the entire range of pressures. Insufficient clamping forces can allow slipping of the sheet between the clamp and base at high stretch ratios and be a source of experimental errors as noted by Hart-Smith and Crisp [22].

As the sample inflates, the original gage length l_0 adopts a curved shape, so that direct measurements of the stretched gage length l_s are not possible. Instead, measurement of the (x, y, z) coordinates of three points, a, b, and c, indicated in Fig.8 enables first computing the radius of curvature and finally the stretched gage length, l_s. The stretch ratio at a given inflation

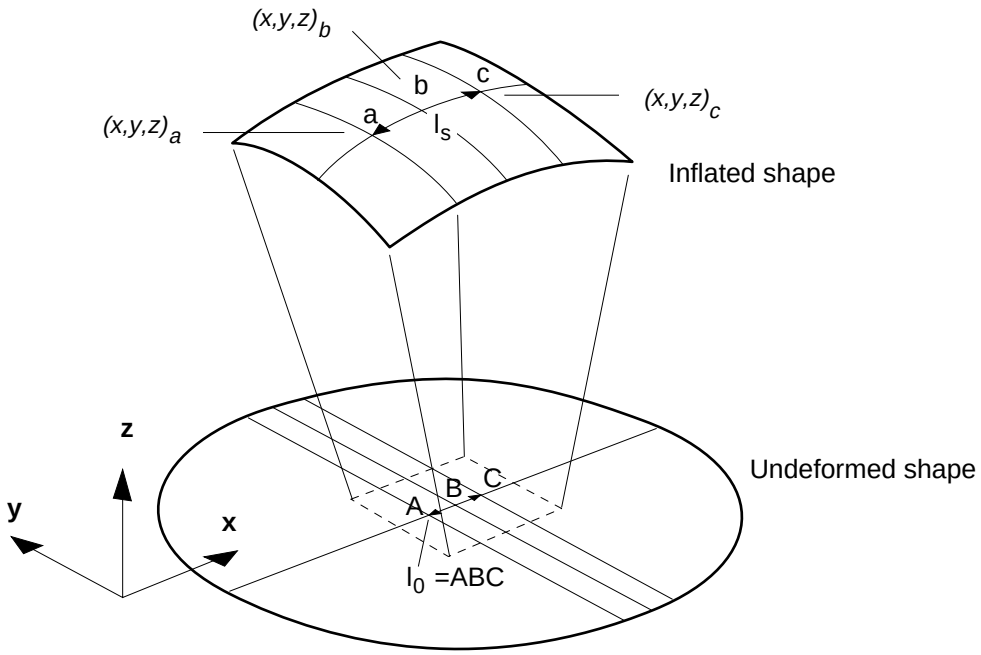

Figure 8: Inflated shape and deformed gage length.

pressure is then

$$\lambda = \frac{l_s}{l_0} \tag{28}$$

It is not absolutely necessary that the deformed gage length be centered at the pole of the inflated shape. The location of point $(x, y, z)_b$ in the neighborhood of the pole is enough to ensure the validity of a biaxial stress state assumption. The ability to track the location of the deformed gage length l_s is more important. The (x, y, z) coordinates were determined by translating the test apparatus under the microscope objective and focusing the crosshairs on the measurement point. The (x, y) values were obtained to $\pm 1\mu$m resolution from the digital readout of linear encoders attached to the microscope stage. The extremely shallow depth of focus of the microscope allowed z-axis measurements repeatable to within $\pm 0.5\mu$m, as taken from a second digital readout attached to the microscope objective's rack. All three coordinate values were written simultaneously to a text file through an RS-232 interface. Pressure values were recorded manually when using the 0-206 kPa (0-30 psi.) Bourdon gage and written to a separate text file when employing the 0-344 kPa (0-50 psi.) pressure transducer. The test procedure is summarized below:

1 - Measure original gage length.

2 - Admit air.

3 - Measure coordinates at three points along the gage length.

4 - Measure pressure.

5 - Repeat steps 2-4 until the preset maximum pressure.

6 - Vent air in steps and repeat measurement to assess hysteresis.

Viton exhibited a noticeable viscoelastic behavior, which complicated testing. Upon a step pressurization, the membrane would not immediately assume an equilibrium position. Before making a measurement, it was necessary to wait between 5 and 30 min. depending on the stretch ratios.

At high pressures, the gage lines tended to blur due to the separation of the ink particles. This made it difficult to locate measurement points through the microscope. In the case of natural latex, the line blurring problem was exacerbated by membrane thinning at high stretch ratios. By Eq.26, the thickness t_s of the latex membrane subjected to the maximum stretch ratio $\lambda_1 = \lambda_2 = \lambda = 4.86$ achieved during the test is

$$t_s = \frac{t_0}{\lambda^2} = \frac{1}{23.6} t_0 = 32.2\mu m \tag{29}$$

($\lambda_3 = t_s/t_0$ where t_0 =0.762 mm was the original undeformed thickness). At this thickness natural latex becomes almost translucent, reducing the contrast of the gage lines. Changing the microscope magnification from 20$\times$ to 5$\times$, and reducing lighting helped to mitigate the problem.

One of the peculiarities of rubber-like materials is the nonmonotonic form of the measured inflation pressure vs. stretch ratio curve, shown in Fig.9 for natural latex. At a certain value

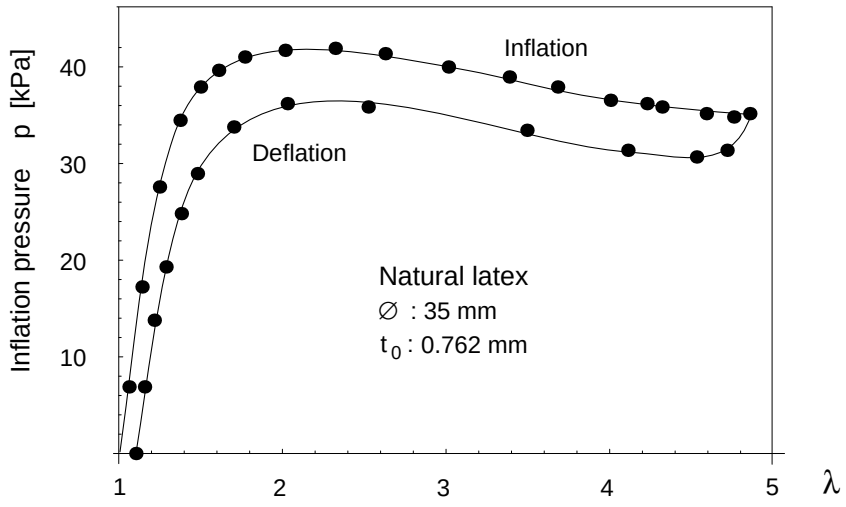

Figure 9: Measured inflation pressure vs. stretch ratio curve for natural latex.

of λ, the addition of air causes the pressure to decrease rather than to increase. The material becomes more compliant and the added air mass is translated into further deformation without

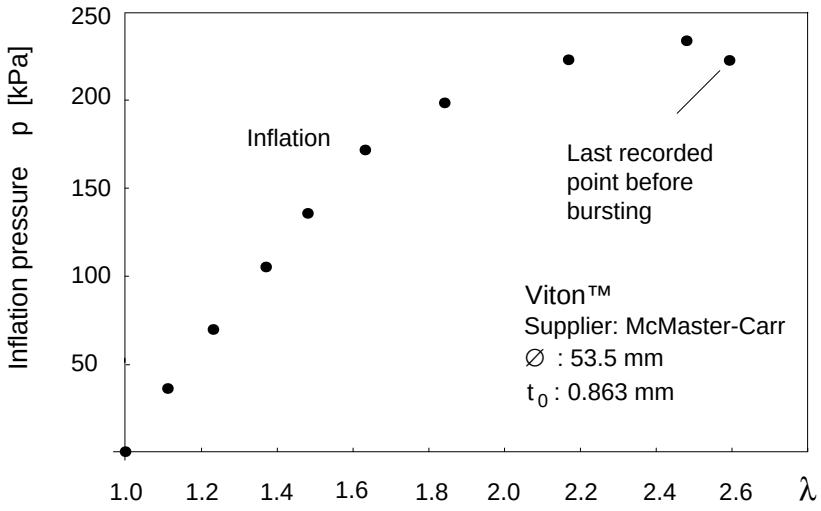

Figure 10: Measured inflation pressure vs. stretch ratio curve for Viton.

raising the internal pressure [8]. As still more air is added, the internal pressure stabilizes and then starts increasing again, indicating less compliance to deformations. This apparent strain hardening is attributed to crystalization phenomena in rubber-like materials [33]. As shown in Fig.10, Viton did not exhibit pressure stabilization, rather it burst shortly after a slight drop in inflation pressure. The non-monotonicity of the inflation pressure represents an unstable bifurcation behavior [9] since more than one stretch ratio is possible for a given inflation pressure [11, 29]. This problem was extensively studied due to its influence on flight prediction of meteorological balloons, Alexander [33] and Needleman [34]. A leak-free test assembly has proven necessary in order to accurately discern the onset of this phenomenon.

3.2 Data Reduction and Calculation of Material Constants

The inflation test yields a series of measurements of grid line mark positions vs. inflation pressure. This data is reduced by the following steps to yield true membrane stress vs. stretch ratios:

1 - convert coordinate measurements to radii of curvature.

2 - calculate of deformed gage lengths using radii of curvature and (x, y, z) coordinates.

3 - calculate stretch ratios.

4 - calculate the biaxial true (Cauchy) stresses in the neighborhood of the measurement points.

[8] This phenomenon is familiar to anyone who has ever tried to inflate a balloon. It is difficult to get the balloon started, but once it reaches a certain size it fills the rest of the way more easily.

[9] See Green and Adkins [9] p.170 for a mathematical proof.

Assuming that the original and deformed gage lengths are coplanar, the radius of curvature r of the curve $a - b - c$ (Fig.11) can be obtained by trigonometric relations as

$$r^2 = \frac{1}{4}\frac{(\Delta x_1^2 + \Delta z_1^2)(\Delta x_2^2 + \Delta z_2^2)[(\Delta x_1 + \Delta x_2)^2 + (\Delta z_1 - \Delta z_2)^2]}{(\Delta x_1 \Delta z_2 + \Delta z_1 \Delta x_2)^2} \tag{30}$$

where all quantities are defined in Fig.11. This was the approach used by Rivlin and Saunders

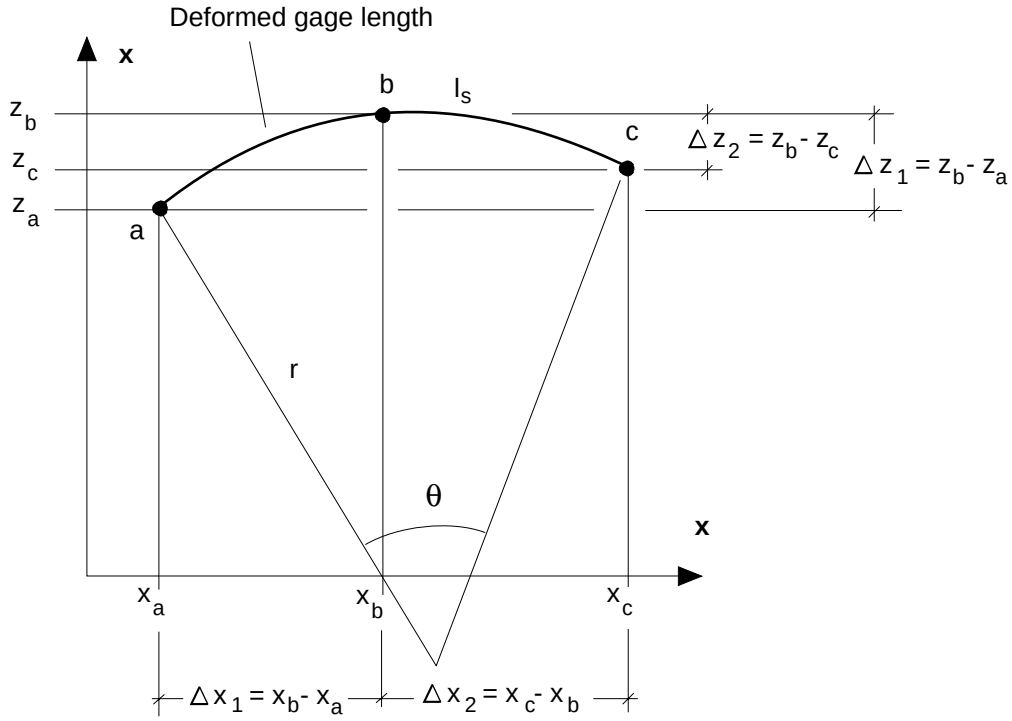

Figure 11: Computation of deformed gage lengths from coordinate measurements.

[14] [10] . The angle θ subtended by the deformed gage length l_s is

$$\theta = 2sin^{-1}\frac{1}{2r}\sqrt{(\Delta x_1 + \Delta x_2)^2 + (\Delta z_1 - \Delta z_2)^2} \tag{31}$$

Since $r >> l_s$ the deformed length l_s can be found as

$$l_s = r\theta \tag{32}$$

And by Eq.28, the stretch ratio is

$$\lambda = \frac{l_s}{l_0}$$

[10] An alternative expression can be derived using shell theory and by assuming a nearly spherical inflated shape [22]

The true stresses in the neighborhood of the pole of the inflated shape can be found from the well-known expression for the stresses in a membrane under uniform pressure,

$$\sigma = \sigma_{11} = \sigma_{22} = \frac{pr}{2t_s} \tag{33}$$

where

σ_{11}, σ_{22} : stresses
p : inflation pressure
r : radius of curvature
t_s : thickness in the deformed state

Except for t_s, all quantities on the right hand side of this expression can be measured or computed. By Eq.29, t_s is a function of the original thickness and the stretch ratio. The stresses are then

$$\sigma_{11} = \sigma_{22} = \frac{pr}{2t_0}\lambda^2 \tag{34}$$

At this point, the experimental data have been converted into pairs of σ vs. λ values. A sample plot obtained for pure gum rubber is shown in Fig.12. The next step is to choose a strain energy function and determine the material constants.

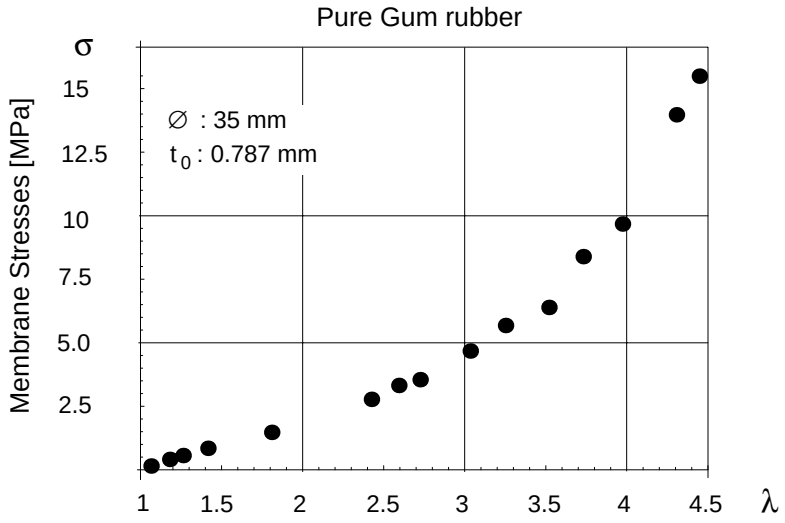

Figure 12: Experimental data points, σ vs. λ for pure gum rubber

We chose the Mooney-Rivlin strain energy function for our study of Viton pads for two main reasons: (a) it is the most commonly used form for which published values are available and (b) the anticipated maximum stretch ratio does not exceed 1.5 for our intended application.

Finding the material constants is a matter of solving an overdetermined system of equations represented by the experimental points. The least squares method provides a means to solve the problem. The usual procedure is to assume any convenient interpolating polynomial and

to calculate the coefficients that minimize the error in fitting the experimental data points such as those indicated in Fig.12. In this case, instead of choosing any function, the analytical expression for the stresses according to Eq.27 is taken as the interpolating function.

$$f(\lambda_j) = 2\left(\lambda_j^2 - \frac{1}{\lambda_j^4}\right) C_{10} + 2\left(\lambda_j^4 - \frac{1}{\lambda_j^2}\right) C_{01} = \sigma_j \tag{35}$$

where

$f(\lambda_j)$: interpolating function
σ_j : jth true stress from the experimental data
λ_j : corresponding stretch ratio

The unknowns are the Mooney-Rivlin constants C_{10} and C_{01}. Note that Eq.35 is linear in C_{10} and C_{01}, which allows the use of a linear least squares procedure (by contrast, Ogden's strain energy function, Eq.21, is nonlinear in the material constants α_i and requires a nonlinear least squares procedure, Twizell and Ogden [35].) The goal is to minimize the following function (see for example, ref.[36] p.258),

$$F(C_{10}, C_{01}) = \sum_{j=1}^{n} [C_{10}\varphi_1(\lambda_j) + C_{01}\varphi_2(\lambda_j) - \sigma_j]^2 \tag{36}$$

where

n : number of experimental data points

and

$$\varphi_1(\lambda_j) = 2\left(\lambda_j^2 - \frac{1}{\lambda_j^4}\right)$$
$$\varphi_2(\lambda_j) = 2\left(\lambda_j^4 - \frac{1}{\lambda_j^2}\right)$$

The points λ_j that comply with Eq.36 must satisfy the conditions

$$\frac{\partial F(C_{10}, C_{01})}{\partial C_{10}} = 0 \qquad \frac{\partial F(C_{10}, C_{01})}{\partial C_{01}} = 0$$

i.e.,

$$2\sum_{j=1}^{n} [C_{10}\varphi_1(\lambda_j) + C_{01}\varphi_2(\lambda_j) - \sigma_j]\varphi_1(\lambda_j) = 0$$
$$2\sum_{j=1}^{n} [C_{10}\varphi_1(\lambda_j) + C_{01}\varphi_2(\lambda_j) - \sigma_j]\varphi_2(\lambda_j) = 0$$

which can be arranged as a system of two linear equations from which C_{10} and C_{01} can be readily obtained,

$$\begin{cases} \left[\sum_{j=1}^{n} \varphi_1^2(\lambda_j)\right] C_{10} + \left[\sum_{j=1}^{n} \varphi_1(\lambda_j)\varphi_2(\lambda_j)\right] C_{01} = \sum_{j=1}^{n} \varphi_1(\lambda_j)\sigma_j \\ \left[\sum_{j=1}^{n} \varphi_1(\lambda_j)\varphi_2(\lambda_j)\right] C_{10} + \left[\sum_{j=1}^{n} \varphi_2^2(\lambda_j)\right] C_{01} = \sum_{j=1}^{n} \varphi_2(\lambda_j)\sigma_j \end{cases} \tag{37}$$

An example of this calculation for pure gum rubber can be found in Appendix B, page 46; the results are plotted in Fig.13 with the fitting function superposed on the experimental data points. Table 1 compares the resulting material constants with those obtained by Oden and

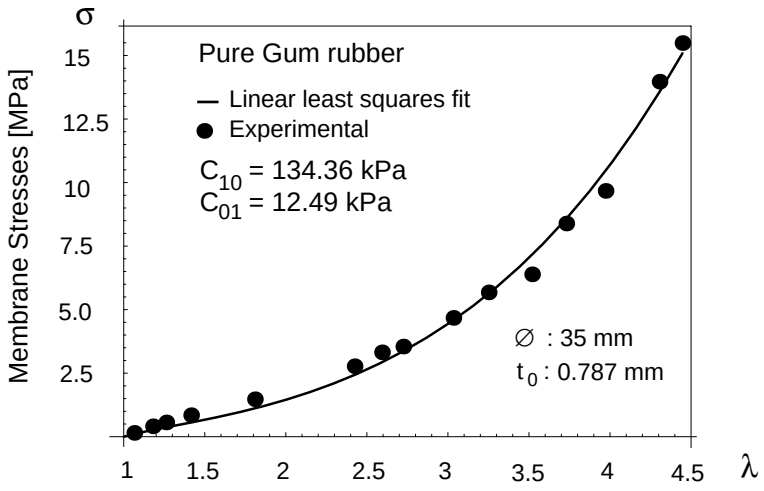

Figure 13: Example of least squares fit of the Mooney-Rivlin form to experimental data.

Kubitza [29] for a similar material. The results are in reasonable agreement in spite of the fact the tests were performed with markedly different specimen sizes.

Table 1
Mooney-Rivlin Constants for Pure Gum Rubber

	C_{10}	C_{01}
Present results (D=35mm, t_0=0.78mm)	134.36 kPa (1.37 kg/cm^2)	12.49 kPa (0.127 kg/cm^2)
Oden-Kubitza[29] (D=381mm, t_0=1.78mm)	111.79 kPa (1.14 kg/cm^2)	13.73 kPa (0.14 kg/cm^2)
D: diameter free to inflate, t_0: initial thickness		

Table 2 **Mooney-Rivlin Constants for Viton™**		
Supplier (dimensions)	C_{10}	C_{01}
McMaster-Carr (D=53.5mm t_0=0.863mm)	1194.6 kPa (12.18 kg/cm^2)	163.0 kPa (1.66 kg/cm^2)
West American Rubber (D=53.5mm t_0=0.838mm)	1329.2 kPa (13.55 kg/cm^2)	263.0 kPa (2.69 kg/cm^2)
D: diameter free to inflate, t_0: initial thickness NOTE: MIL-R-83248 Type 2, class 1 material specifications		

Table 2 shows the material constants for MIL-SPEC grade Viton test samples obtained from two different vendors. These values turned out to be considerably higher than the constants for pure gum rubber. A third commercial-grade Viton sample was not tested due to its extremely low elongation at break (estimated at less than 130%) and its chemical susceptibility to the solvent-based marker used to trace the gage lines.

The values for C_{10} and C_{01} listed for the first sample of Viton were checked with a simple four-element finite element model of a flat sheet intended to simulate the zone near the pole of

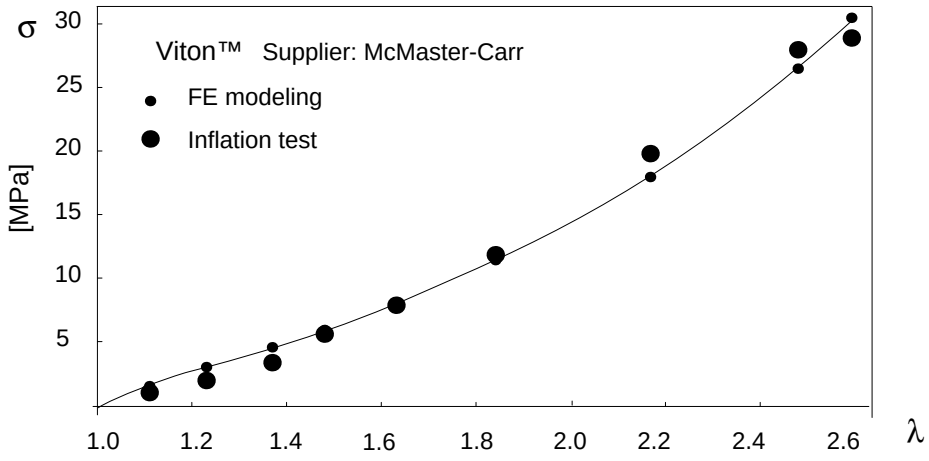

Figure 14: Comparison of experimental data with a finite element model.

the inflated shape (by neglecting again curvature effects). A series of prescribed displacements in two orthogonal directions were imposed in steps to reproduce the values of stretch ratios obtained from the test data. A comparison of the true stress vs. stretch ratio evolution obtained both from the finite element modeling and the experimental data is shown in Fig.14. This simple check served as a qualification of the finite modeling with the experimentally obtained data. The validity of the Mooney-Rivlin constants is of course limited to the loading mode from which they were derived. In the present investigation of a flat pad under compression,

these constants are assumed to be valid as long as the deformation remains "as homogeneous as possible."

4 Finite Element Modeling of the Proposed Shapes

A commercial finite element modeling program, Abaqus v.5-2 [37], was chosen to qualify our experimental results and to evaluate proposed pad designs. Abaqus includes strain energy functions valid for several hyperelastic constitutive models:

- Mooney-Rivlin's form (Eq.10)
- Second order deformation form (Eq.15)
- Ogden's form (Eq.21)

It also includes the Neo-Hookean form since it can be obtained as a particular case of the Mooney-Rivlin form with $C_{01} = 0$. Ogden's strain energy function can be formulated with up to a six term (n=6) approximation of Eq.21. In addition, any of the constitutive models presented previously can be included through a user-defined subroutine (`UHYPER`).

A Digital Equipment Corporation Alpha AXP-based workstation was used to run all finite element models. Typical CPU times ranged from a few minutes to several hours depending on the loading level and degree of mesh refinement. With the exception of a few simple models, Patran v.3 [38] was used for mesh generation.

4.1 Model Description

The pressure pad problem was modeled with the following assumptions,

1 - Perfect adhesion of the pad faces to the compressing surfaces (once in contact, the pad faces do not separate). This assumption is usually valid for the high pressure die attach process where one side the pad is held by the rough active surface of the die and the other side is glued to the pressure plate (see Fig.1).

2 - Constant load applied by the compressing surfaces (as opposed to constant normal tractions).

3 - Perfect rigidity of the compressing surfaces. This assumption is not strictly valid for the high pressure die attach process in which the adhesive acts as an elastic foundation below the die, Fig.1.

A typical mesh used to model a square pad with a central hole will be used as an example to describe the finite element modeling. A three-dimensional model was adopted since the objective was to study contact stresses and visualize their distribution on the pad faces. Due to the symmetry of the geometry, boundary conditions, and loads, the modeling can be done on one eighth of the actual square pad. The effect of the rest of the pad can be modeled by imposing the appropriate boundary conditions to the model as indicated in Fig.15. The midsurface nodes are constrained to remain on the same $x - y$ plane at all times during the loading history (when u_z displacements occur, these nodes move as a whole, but independent movements in the x and y directions are still possible). Again, by symmetry considerations only one of the rigid compressing surfaces is modeled.

Three-dimensional eight-node linear-interpolation mixed-formulation elements were used

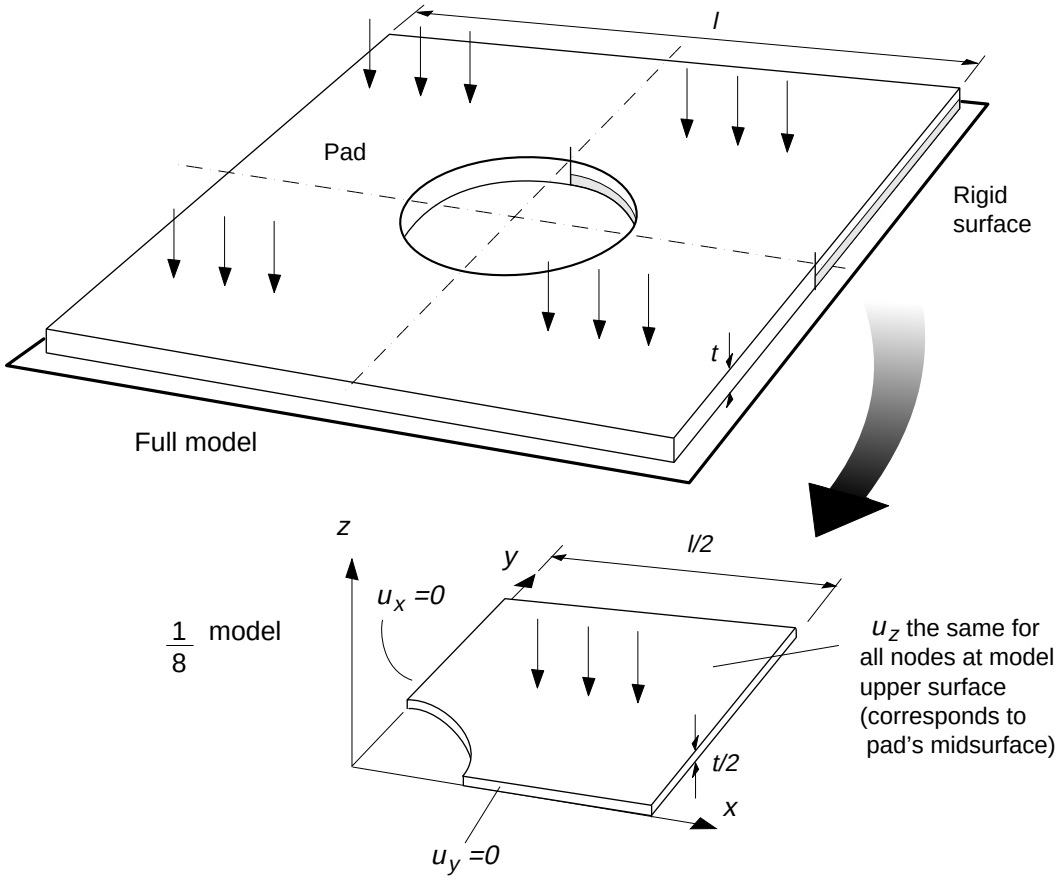

Figure 15: Pressure pad modeling and boundary conditons.

throughout the modeling (Abaqus element type `C3D8H`). When necessary, six-node mixed-formulation triangular prism elements (Abaqus element type `C3D6H`) were used as mesh fillers. The use of these mixed-formulation elements were mandated by the incompressibility of rubber-

like materials for which the stresses cannot be uniquely determined from the displacements [11]. Three hundred and ninety 3-D elements were defined for the example in Fig.16. Only three elements were used along the thickness to maintain an adequate aspect ratio in the entire model. The height of all elements were the same, but an alternative "pre-distorted" mesh for extremely high loads may consider unequal element heights. Such a mesh is generated in a way that "negates" unfavorable distortions under loads, by making the original element shapes as if they were deformed in the opposite direction.

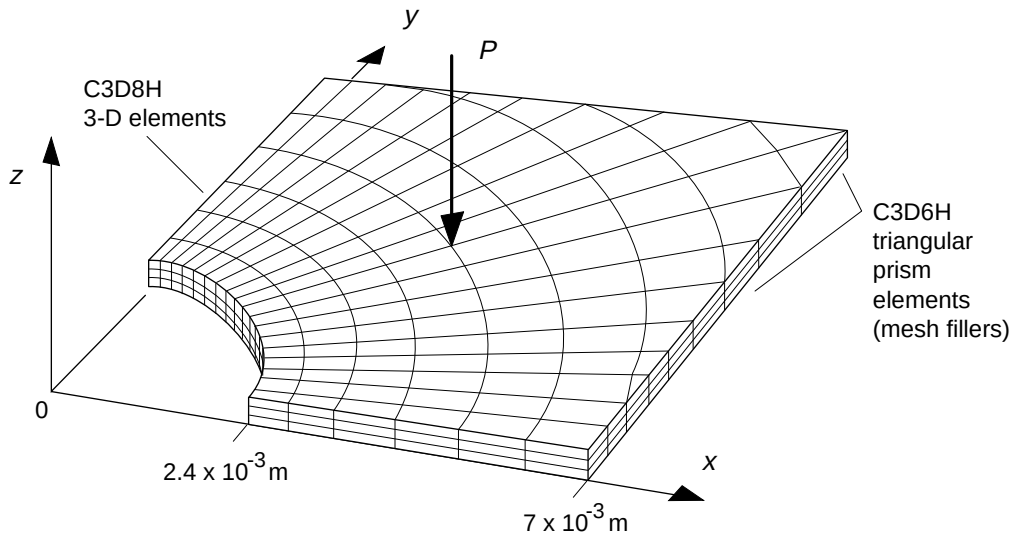

Figure 16: Mesh modeling a pad with a central hole.

A different type of element was used to model the interaction of the lower pad face with the rigid compressing surface. The three dimensional `C3D8H` elements in the mesh of Fig.17 were overlaid on the lower surface with interface elements `IRS4` capable of detecting contact with a separately defined rigid surface. The lateral edges were also covered with interface elements to model possible bulging and contact with the rigid surface. However, only two rows of lateral interface elements were defined. The `C3D8H` elements adjacent to the midsurface of the actual pad (upper surface of the model) did not include them due to the kinematic constraint defined on its constituent nodes (they always remain in the same $x - y$ plane). If interface elements were defined there, the contact force would become undetermined if actual contact occured. Fortunately, extreme lateral bulging was not expected to occur with the loads of the case under study (if it were, the problem could be solved by defining more elements along the thickness). Interface elements also have the ability to deform with the 3-D elements to which they are attached and thus give the true (Cauchy) contact stresses on the rigid surface. The plots shown in the next subsection that describe the distribution of contact stresses are actually describing

[11] Traditional displacement-based elements have only displacements as field variables and calculate stresses from displacement gradients. Such elements cannot model rubber-like materials since they can be subjected to stresses with no nodal displacements. Mixed formulation elements have both stresses and displacements as field variables.

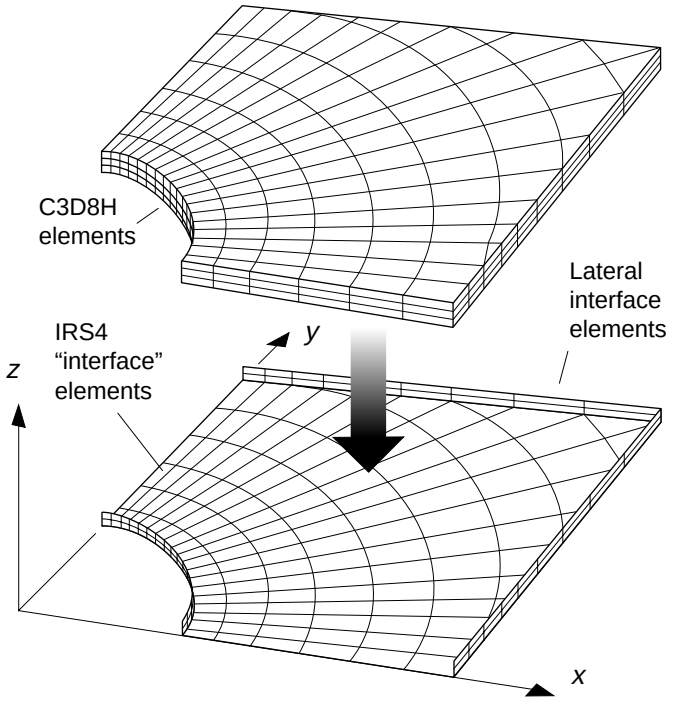

Figure 17: Use of interface elements to detect contact stresses.

tractions applied by the rubber pad to the interface elements. Friction between the interface elements and the rigid surface was considered to be infinite (perfect adhesion) but could have been modeled with any values from 0 to ∞.

A concentrated constant load P was applied in the $-z$ direction to the upper surface of the mesh (midsurface of the actual pad), Fig.16. This load was automatically considered by Abaqus as uniformly distributed over the entire upper surface due to the kinematic constraint of its nodes (which are prescribed to remain in the same $x-y$ plane).

The model depicted in Fig.16 consists of 610 nodes and 592 elements including the interface elements and has an RMS wavefront of 395 after internal optimization performed by Abaqus. The input file corresponding to this example is included in Appendix C, page 47.

4.2 Finite Element Modeling Results

Due to the kinematic constraints imposed by a large friction coefficient, the contact stresses originated by the compression of a solid rubber pad against a rigid surface are nonuniform, as shown in Fig.18(a). This plot was obtained by modeling one eighth of a 14×14 square by 0.8mm thick solid sheet of Viton subjected to uniform compressive tractions of 400 kPa and using the Mooney-Rivlin constants for the first sample material of Table 2 (C_{10}= 1194.6 kPa, C_{01}= 163 kPa). The contact stresses have a peak value of 816 kPa at the center of the pad and

decrease toward the edges reaching a value of 71.3 kPa at the corners [12] . The distribution of contact shear stresses in the *x*-axis direction is also nonuniform as shown in Fig.18(b). In this case there is a sign reversal, with a peak contact shear stress of +85.6 kPa at the right edge and a minimum of -207 kPa along the vertical axis. Note that there are also contact shear

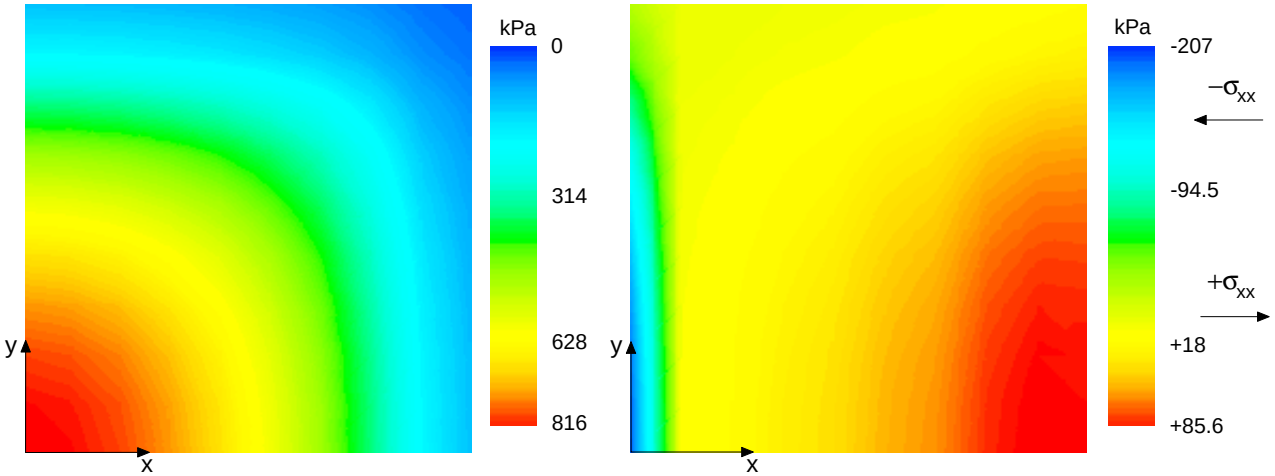

(a) (b)

Figure 18: Normal (a) and shear (b) contact stresses applied by a $14\times14\times0.8$mm solid Viton pad. One-eighth finite element model with a 19.6 N normal load (uniform compressive tractions of 400kPa).

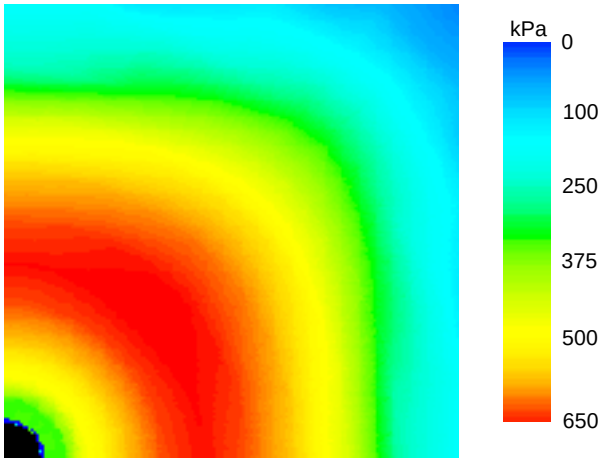

Figure 19: Distribution of normal contact stresses in a $14\times14\times0.8$mm perforated pad. Hole diameter: 1.2mm. One-eighth finite element model with a 19.6 N normal load.

stresses in the *y*-axis direction, whose distribution is the mirror image of Fig.18(b). Therefore, the true peak values differ from these values and must be found pointwise by performing the

[12]The contact stresses reported here follow Abaqus' sign convention in which tractions and stresses are positive if they act "against" a surface and negative if they "pull" away from a surface. For example, a rubber ball subjected to hydrostatic compression is modeled in Abaqus with positive tractions. Therefore, a positive contact stress means tractions acting "against" a rigid surface. Note that this is opposite to the convention used in elasticity theory.

corresponding transformation. An upper bound on the true peak value is $\sqrt{2}$ times the maximum contact shear stress along a given axis. The signs refer to the direction of the contact shear stresses, positive along the $+x$ direction and negative otherwise. At this load, the amount of lateral bulging at the midsurface of the pad is minimal ($7.6 \times 10^{-}3$ mm). The mesh used to model the solid pad is shown in Fig.20. It models one-eighth of the pad and consists of 162 three-dimensional `C3D8H` elements and 99 `IRS4` interface elements. The normal load applied to the upper surface of the model (midsurface of the actual pad) was 19.6 N, which is equivalent to 400 kPa when distributed over the entire model's surface.

As noted on page 11, the introduction of a small through hole in the pad relieves the normal contact stresses in its vicinity since the surrounding material is able to deform with relative freedom. If only one hole is placed in the center of the pad while maintaining the same normal load and pad dimensions, the distribution of normal contact stress changes as shown in Fig.19. With a hole of 1.2mm in diameter, the region of peak stresses shifts to a roughly annular zone

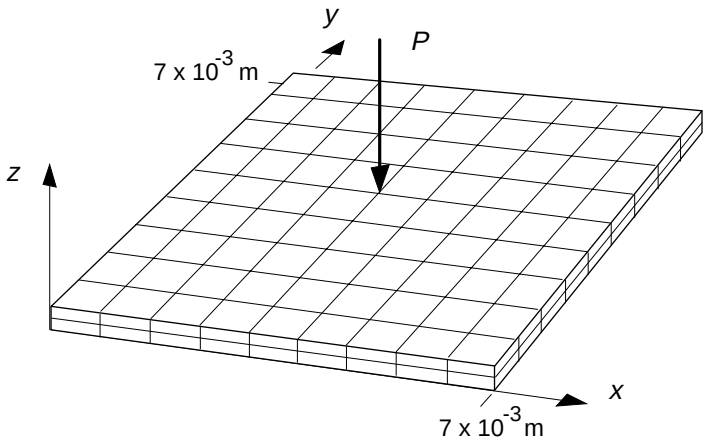

Figure 20: Mesh modeling a solid square pad.

surrounding the central hole and the maximum value drops 20% to 650 kPa. Note that the normal load applied to the finite element model was the same used for the solid square pad (19.6N) which implies that the average stress is higher than the previous case due to the loss of cross sectional area at the hole. By contrast, the peak values for contact shear stresses increase to +104 kPa and -606 kPa. The finite element model used for this case is similar to the one described in section 4.1. The hole diameter can be increased with a slight reduction of the peak normal contact stress but eventually it begins to increase again due to the effect of the reduced cross sectional area.

Further reductions in the normal contact stresses can be achieved with a multi-hole approach. Four holes can be arrayed symmetrically about the center of the pad as indicated in Fig.21. The maximum contact stress with the same normal load decreases to 589 kPa, 28% less than for the original unperforated pad.

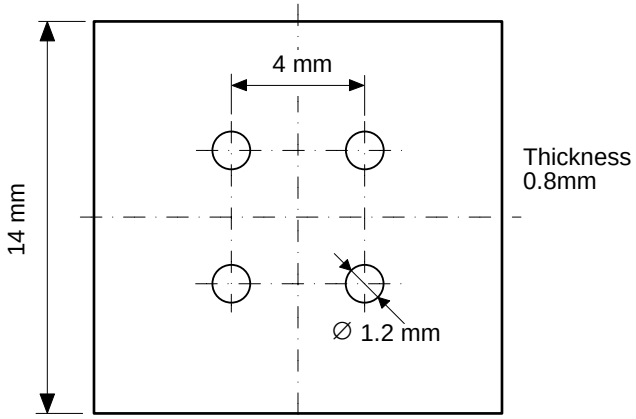

Figure 21: Pad perforated with a symmetrical array of four holes.

		Hole Diameter		
# holes	Location (x,y) mm	1.2mm	2.4mm	4.8mm
4	(3.5,3.5)	993 kPa -217 +216	1160 -251 +241	1780 -340 +398
4	(2.6,2.6)	831 -427 +216	779 -370 +223	893 -328 +349
4	(2,2)	589 -335 +182	667 -218 +177	
1	(0,0)	650 -606 +104	638 -317 +116	682 -212 +151
0		No hole 816 -207 +85		

Peak normal contact stress (σ_{zz})

Max. and Min. shear contact stress [kPa] (σ_{xx})

Figure 22: Comparison of peak normal and shear contact stresses for different hole diameters and placement.

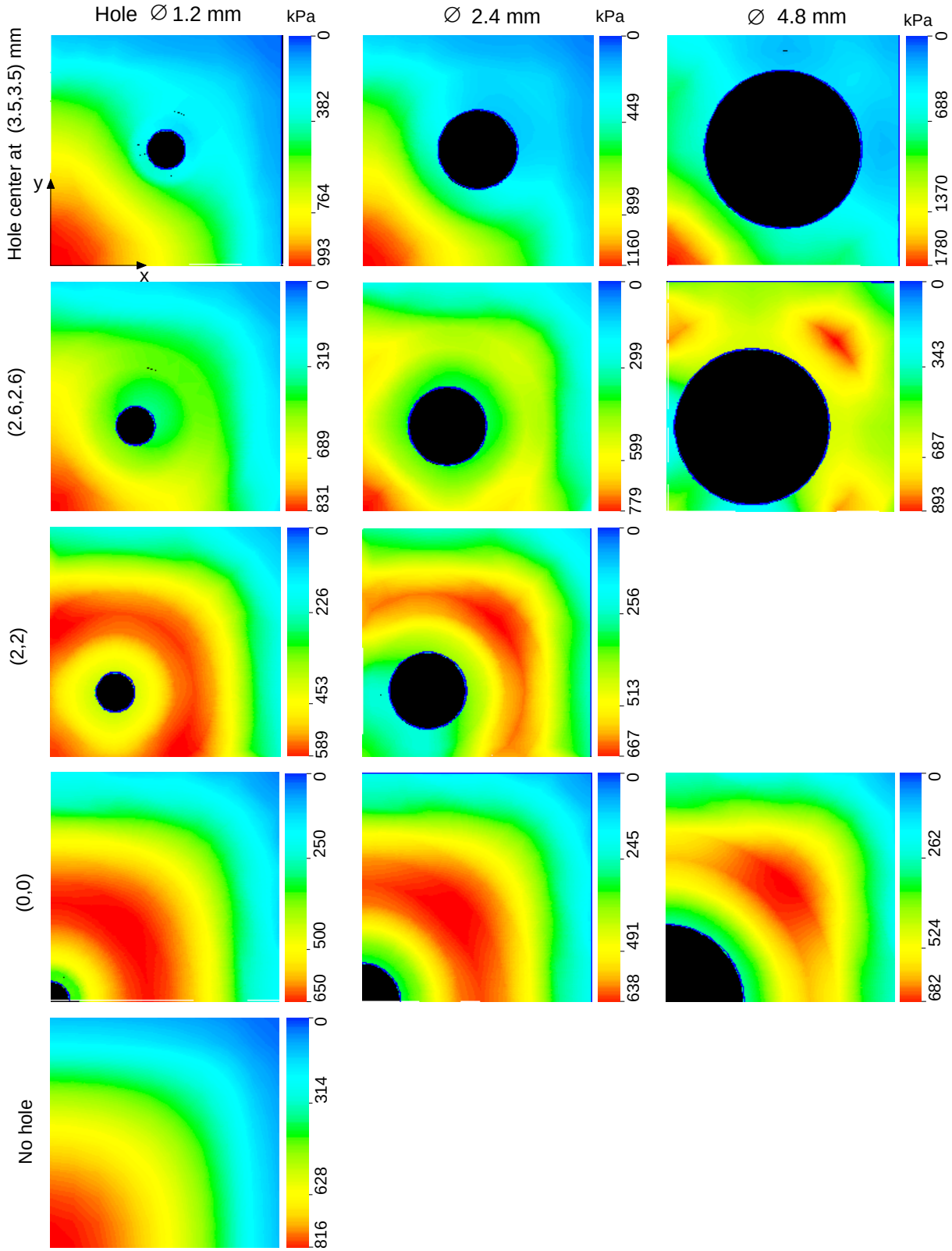

Figure 23: Normal contact stresses for various hole diameters and placement

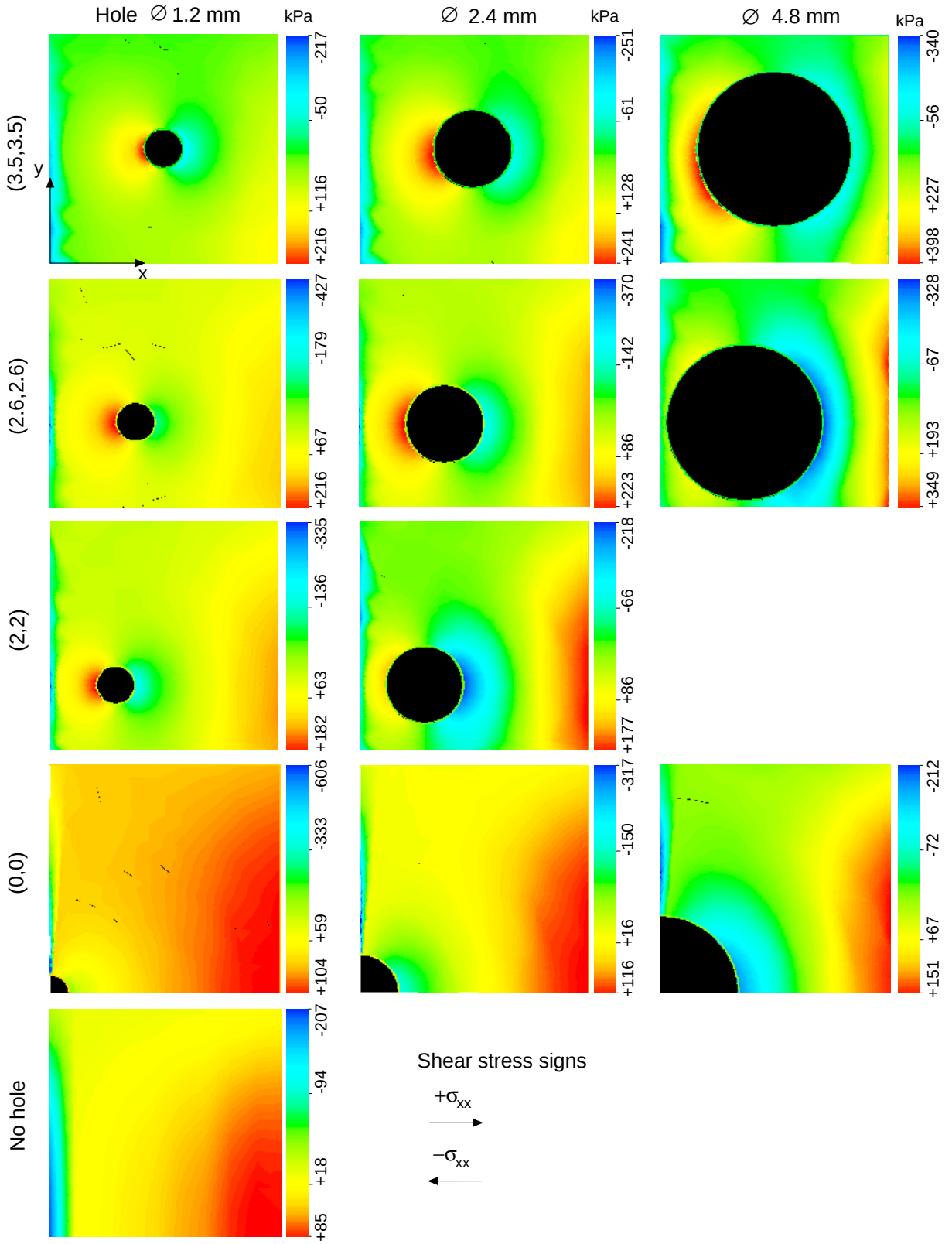

Figure 24: Shear contact stresses for various hole diameters and placement

For a symmetrical four-hole array, the placement as well as the diameters of holes can be changed. Peak normal and shear contact stresses for all cases are summarized in Fig.22. Complete plots for normal and shear contact stresses are shown in Figs.23-24. It is noted that no attempt has been made to consider viscoelastic effects in the finite element modeling. Therefore, the long term values of the peak contact stresses are predicted to fall from the values listed in Fig.22 when a viscoelastic constitutive model is included. However, the stress values predicted without considering viscoelasticity are still valid as upper bounds in any given design.

5 Experimental Verification

To verify our finite element modeling of Viton pad deformation and contact stress distribution, and to investigate the effect of interfacial friction, we built a pad test apparatus that allowed

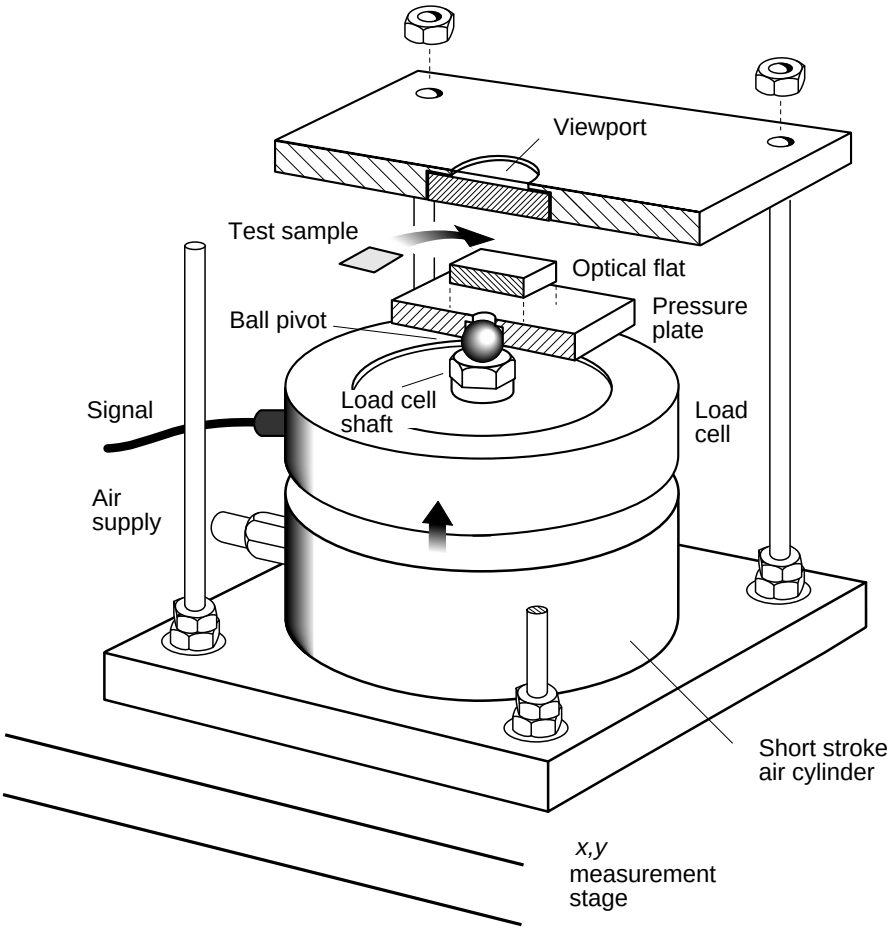

Figure 25: Pad test apparatus.

direct observation and measurement of samples under a specified load (Fig 25). Like the inflation test apparatus, the entire pad test assembly fit on the calibrated stage of our universal microscope. An air cylinder with a pressure-regulated source supplied the required load. A 0

to 4450 N load cell attached to the piston gave a direct indication of the load. The load cell contacted a ball on the pressure plate assembly, the ball serving to center the load on the sample pad without lateral thrust. A piece of glass was bonded to the pressure plate. The sample pad was then placed on the optically flat surface of the glass. A second piece of glass covered the pad. This 28 mm square $\times$ 5 mm thick viewing glass was optically flat on both surfaces. It was held in place by a pocket in an aluminum plate with a viewing hole in the center. The pad could be aligned with the center of the assembly by looking through this viewing port and the glass.

As the air pressure was turned up and the pad was squeezed, the deformations could be measured through the glass by the microscope and its x, y, z positioning stage.

For some experiments, the contacting surfaces were coated with glycerin to minimize interfacial friction. For others, to approximate a large friction coefficient, the contacting glass surfaces were blasted with aluminum oxide. Prior to grit blasting, the viewing glass was masked at 12 places with 0.8 mm wide strips of tape. These strips crossed the pad edge at a right angle, beginning 1mm inside the original pad outline. This minimized the effect of low friction near the measurement location.

Measurements were taken at the corners and at several edge locations while the load was incrementally increased up to roughly 1000N. The bulging edge of the pad was used for the point of measurement in all cases where it could be seen clearly. With a large friction coefficient, the contacted edge of the pad did not move significantly, and visible deformation was limited to edge bulging. For the glycerin cases, the bulge was not significant and therefore, the contacted edge of the pad was measured.

A $15\times15\times0.86$mm Viton pad with a 4.7mm diameter center hole was coated with glycerin, tested with a 890N load, and results compared with a finite element model that assumed a zero friction coefficient. The corners moved 1.89mm, versus the predicted 2.27mm, and the midpoints of the edges moved an average of 1.40mm versus the predicted 1.609mm, Fig.26. The central hole shrank approximately 1mm in diameter during the test, while the finite element model predicted a 1.03mm increase in diameter. The agreement within 20% for the edge displacements seemed reasonable since the actual coefficient of friction was certainly larger than zero, as evidenced by the dissimilar behavior at the central hole.

The same test was conducted using the grit blasted glass surfaces with a 1183N load to simulate a large friction coefficient. In this case, the measurements correspond to the outline of the bulging edges. The midpoints moved an average of 0.252mm versus the 0.141mm predicted by finite element modeling assuming an infinite friction coefficient. By contrast, the corners exhibit a wide variation between experimental and predicted displacements as shown in Fig.27. The experimental errors were certainly larger in this test due to the small magnitude of the measured displacements and the uncertainty about the value of the actual friction coefficient.

A qualitative test was run to determine the degree of agreement of the finite element model's normal contact stress results with the actual pads. A "pressure indicating" paper was used to record the normal contact stresses originated by compression of test pads. This paper consists

of two coated polyester sheets assembled face-to-face [13] . The first sheet is coated with a microencapsulated dye and the second with a color developing layer. The microcapsules break

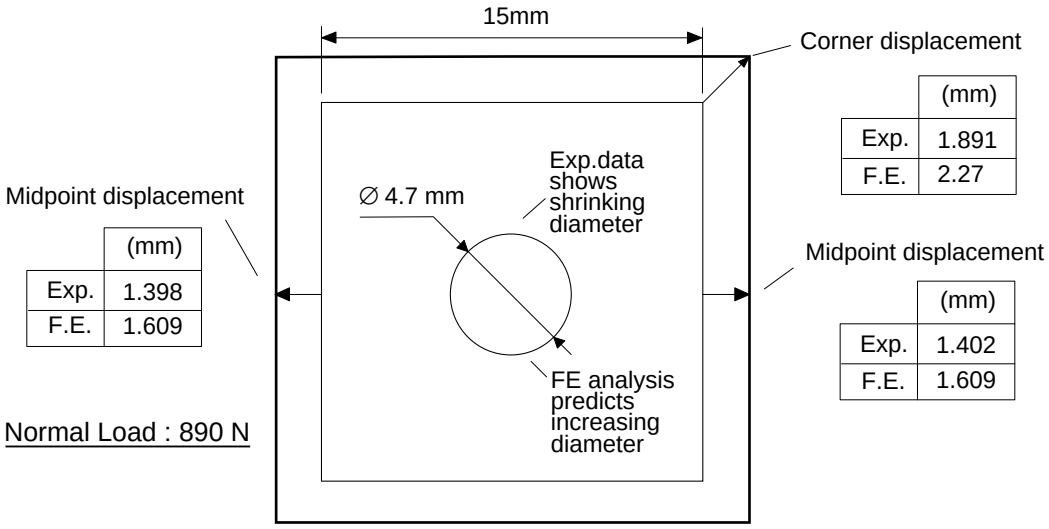

Figure 26: Comparison of experimental and finite element displacements in a perforated Viton pad with glycerin (small friction coefficient)

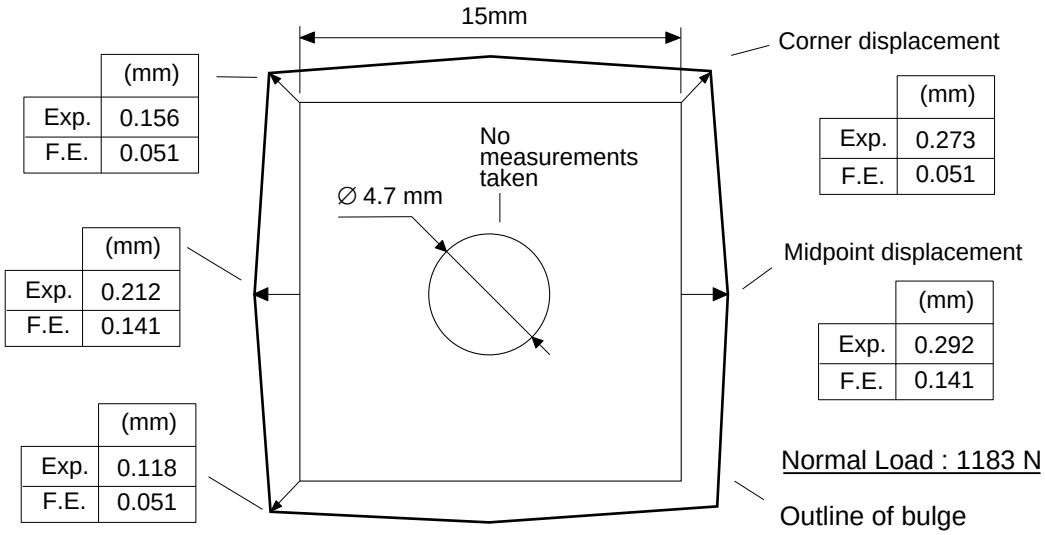

Figure 27: Comparison of experimental and finite element displacements in a perforated Viton pad, large friction coefficient

in a controlled fashion when the film is compressed, leaving an image with intensity proportional to the local pressure. While quantitative measurements are possible with a densitometer, we limited our evaluation to qualitative comparisons. Several film types are offered, we chose the

[13] Pressurex (Fuji) pressure indicating film, supplied by: Sensor Products, Inc., East Hannover, NJ.

"SL" grade, with a 480-2400 kPa pressure range. The paper was placed between the pad and the viewport. A load of 1000N was applied and photographs taken. Three $14\times14\times0.8$mm square pad designs were tested: pad with no holes, pad with one 2.4mm diameter central hole, and pad with four 1.2mm diameter holes arranged in a 4mm square grid (see Fig.21). The test load was determined to impose average compressive tractions of 5 MPa over the unperforated 14×14mm square pad. The experimental results are shown in Fig.28 and the corresponding finite element results under a 996N load in Fig.29.

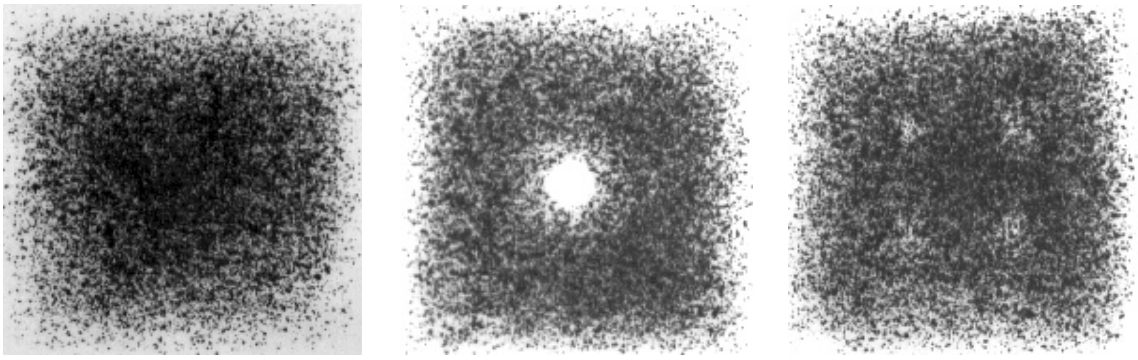

(a) (b) (c)

Figure 28: Normal contact stresses registered by a pressure indicating paper on three pad designs. (a) No hole, (b) one 2.4mm diameter hole, and (c) four 1.2mm diameter holes. Normal load: 1000N, pad dimensions: $14\times14\times0.86$mm, supplier: McMaster-Carr

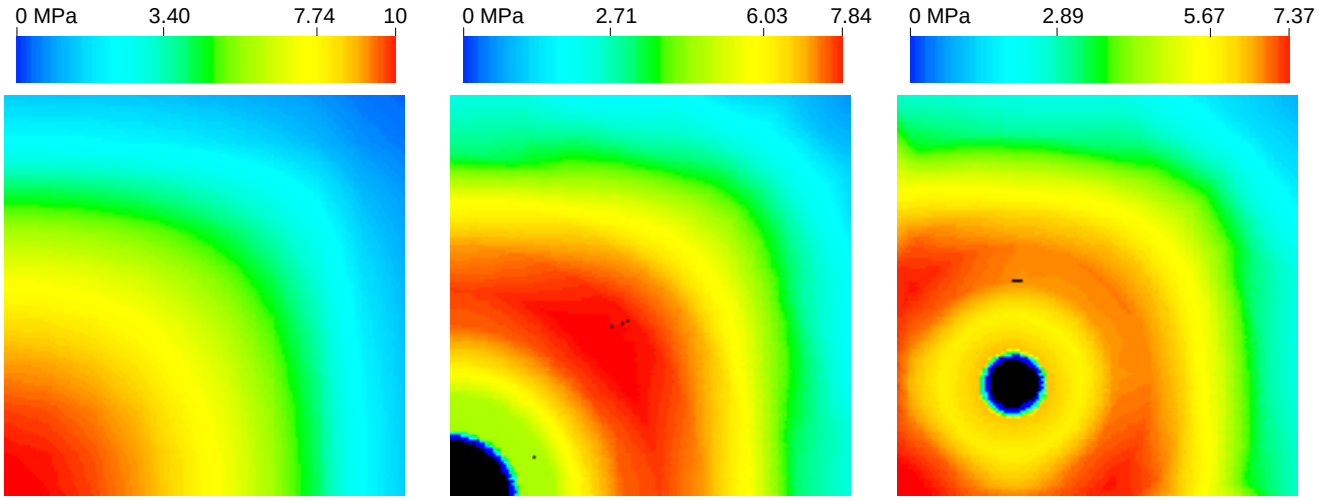

Figure 29: Normal contact stresses from a finite element analysis of the three pad designs of Fig.28. Normal load of 996N in all cases.

Experiment and prediction are in good qualitative agreement. The pad with no holes has normal contact stresses that are high at its center, and very low at the edges. Adding a single center hole shifts the region of normal contact stresses to the surrounding region as predicted

by finite element modeling. Low contact stresses are evident next to the edge of the hole. Four holes spread the contact stresses out more uniformly. The edge of the pad has a reasonable value of contact stresses.

6 Conclusions

Elastic properties of gum rubber, natural latex, and Viton were obtained using experimental methods. Inflation tests were conducted to derive material constants for a Mooney-Rivlin constitutive model. This correlated well for modest deformations in the case of Viton. The results were used in a finite element model to evaluate flat, perforated pressure pads for microelectronic applications. Properties of the Viton samples tested varied significantly with supplier.

Using the Mooney-Rivlin strain energy function, finite element methods were used to study pad deformations under compression and the corresponding distribution of contact stresses on a rigid surface. A number of competing perforated pad designs were evaluated. For the base case, a solid 14mm square by 0.8mm thick pad, the maximum normal contact stress occurred at the center with a peak value of more than twice the average over the entire pad.

Pad deformations under load were measured optically, compared with the displacements of a finite element model, and found to be in reasonable agreement. Uncertainty of interfacial friction was the largest component of this error. Direct measurements of the pads' normal contact stress distributions were made using a pressure-indicating film. These tests showed good qualitative agreement with the finite element modeling.

Judicious perforation of flat pads was found to greatly reduce the variation and maximum value of normal stresses. Our preferred design for a 14 mm square by 0.8 mm thick Viton pad, used four 1.2 mm holes symmetrically arrayed in a 4 mm square grid, centered on the pad (Fig.21). Compared to an unperforated pad, the finite element modeling indicated a 28% reduction in the maximum normal contact stress. However, this reduction was obtained at the expense of an increase in the contact shear stresses. While a great deal of intuition was gained in the course of this work, detailed finite element models are still required to truly optimize pad perforation patterns.

7 Acknowledgments

The authors wish to thank Wayne Mack for his work on the data acquisition equipment, Annie Warren and Colleen Hawk for their efficient system administration, Joel Bartlett for his invaluable contribution on color graphics capture, and Amitabh Srivastava for his aid in formatting this report.

Appendix A

Deformation Measures in Finite Elasticity Theory

Following is a brief development of deformation and its measures in finite elasticity theory. For a more thorough treatment, see [8, 39]. To derive measures of deformation in finite elasticity, consider a collection of points in an initially unstressed configuration indicated by C_0 in Fig.30. After a finite deformation, this same collection of points occupies configuration C_1. Points in the two configurations are referenced to different coordinate systems, X_i for the

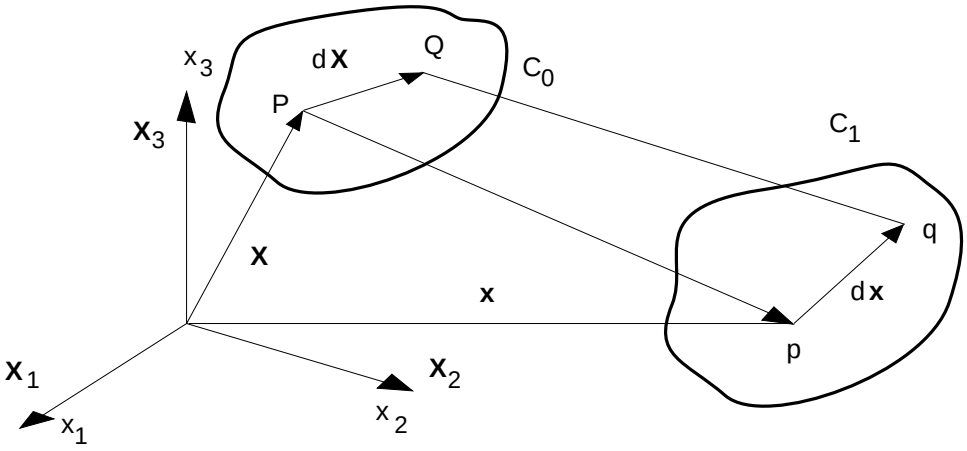

Figure 30: Initial and final configurations

initial state and x_i for the deformed state. The description of the deformation will depend on the reference configuration chosen for the analysis. If the Lagrangian description is chosen, the attention is centered on what happens to a point say initially at P. By contrast, the Eulerian description emphasizes what happens at a particular point in space such as p. Both configurations, undeformed and deformed, are related by a mapping $\boldsymbol{\Xi}$ between corresponding position vectors that can be expressed as [8, 39]

$$\boldsymbol{x} = \boldsymbol{\Xi}(\boldsymbol{X}) \tag{38}$$

where

$\boldsymbol{X}$: position vector of a point in the undeformed configuration
$\boldsymbol{x}$: position vector of the same point after a deformation

By convention, quantities associated with the undeformed configuration are capitalized. A particular relative length, e.g. PQ, is defined by its differential length

$$d\boldsymbol{X} = dX_A \boldsymbol{I}_A \tag{39}$$

where

$\boldsymbol{I}_A$: basis vector of the undeformed configuration

After a deformation, the relative length between the homologous points, p and q, can be described in the deformed configuration basis as

$$d\boldsymbol{x} = dx_i \boldsymbol{i}_i \tag{40}$$

where

$\boldsymbol{i}_i$: basis vector of the deformed configuration

The differential quantity dx_i can be expressed as

$$dx_i = \frac{\partial x_i}{\partial X_A} dX_A = x_{i,A} dX_A \tag{41}$$

where $x_{i,A}$ indicates derivatives with respect to X_A and is called deformation gradient tensor ($x_{i,A} = F_{i,A}$). Similarly,

$$dX_A = \frac{\partial X_A}{\partial x_i} dx_i = X_{A,i} dx_i \tag{42}$$

A measure of deformation can be expressed by the difference of the squares of the differential lengths, i.e.,

$$(dx_i)^2 - (dX_A)^2 = dx_i dx_i - dX_A dX_A \tag{43}$$

This expression can be put in terms of the undeformed configuration by substituting Eqs.40 and 41,

$$\begin{aligned} (dx_i)^2 - (dX_A)^2 &= (x_{i,A} dX_A)(x_{i,B} dX_B) - \delta_{AB} dX_A dX_B \\ &= (x_{i,A} x_{i,B} - \delta_{AB}) dX_A dX_B \\ &= (C_{AB} - \delta_{AB}) dX_A dX_B \end{aligned} \tag{44}$$

where

δ_{AB} : Kroenecker delta

C_{AB}: Green deformation tensor

The symmetric tensor E_{AB} defined by

$$2E_{AB} = C_{AB} - \delta_{AB} \tag{45}$$

is the Lagrangian deformation tensor.

The same deformation measure (Eq.43) can be expressed in terms of the deformed configuration as well,

$$\begin{aligned} (dx_i)^2 - (dX_A)^2 &= (dx_i dx_j \delta_{ij}) - X_{A,i} X_{A,j} dx_i dx_j \\ &= (\delta_{ij} - c_{ij}) dx_i dx_j \end{aligned} \tag{46}$$

where

δ_{ij} : Kroenecker delta

Now, c_{ij} is the Cauchy deformation tensor and e_{ij} the Eulerian finite deformation tensor,

$$\begin{aligned} c_{ij} &= X_{A,i}X_{A,j} \\ 2e_{ij} &= \delta_{ij} - c_{ij} \end{aligned} \tag{47}$$

Note that this tensor is completely described by the subscripts associated with the current (deformed) configuration.

The use of these tensors is dictated by the purpose of a specific application. Alternative measures of deformations may be based on the stretch ratios, defined in the current configuration as

$$\frac{1}{\lambda_{\boldsymbol{n}}} = \frac{dX}{dx} \tag{48}$$

where

$\lambda_{\boldsymbol{n}}$: stretch ratio along $\boldsymbol{n}$
dX : original relative length
dx : current relative length

The subscript in $\lambda_{\boldsymbol{n}}$ indicates that the stretch ratio is associated with a particular direction aligned with the unit vector $\boldsymbol{n} = d\boldsymbol{x}/dx$ referenced to the current configuration. The same quantity can be defined in the original configuration along the unit vector $\boldsymbol{N} = d\boldsymbol{X}/X$ as

$$\Lambda_{\boldsymbol{N}} = \frac{dx}{dX} \tag{49}$$

where

$\Lambda_{\boldsymbol{N}}$: stretch ratio along $\boldsymbol{N}$

In the particular case where the deformation is such that both $\boldsymbol{N}$ and $\boldsymbol{n}$ are pointing in the same direction, both stretches are the same and can be treated much in the way as the engineering strain was defined in Eq.1.

Even though stretch ratios were not specifically defined as tensorial quantities, they can be considered as such due to their relationship with the Green and Cauchy deformation tensors given by [39],

$$\begin{aligned} \frac{1}{\lambda^2_{\boldsymbol{N}}} &= \boldsymbol{n} \cdot \boldsymbol{c} \cdot \boldsymbol{n} \\ \Lambda^2_{\boldsymbol{N}} &= \boldsymbol{N} \cdot \boldsymbol{C} \cdot \boldsymbol{N} \end{aligned} \tag{50}$$

where

$\boldsymbol{C}$: Green deformation tensor
$\boldsymbol{c}$: Cauchy deformation tensor

This implies that the invariants of the Green and Cauchy deformation tensors are also the invariants of the stretches. Assuming homogenous deformations where the orientation of the unit vectors ($\boldsymbol{N}$ and $\boldsymbol{n}$) do not change, both stretch measures are the same and can be stated as

$$\overline{\boldsymbol{\lambda}} = \boldsymbol{\lambda}\boldsymbol{\lambda} = \begin{bmatrix} \lambda_1^2 & 0 & 0 \\ 0 & \lambda_2^2 & 0 \\ 0 & 0 & \lambda_3^2 \end{bmatrix} \tag{51}$$

Its invariants are expressed as,

$$\begin{aligned} I_1 &= tr[\overline{\boldsymbol{\lambda}}] = \lambda_1^2 + \lambda_2^2 + \lambda_3^2 \\ I_2 &= (tr[\overline{\boldsymbol{\lambda}}])^2 - (tr[\overline{\boldsymbol{\lambda}\boldsymbol{\lambda}}]) = \lambda_1^2\lambda_2^2 + \lambda_2^2\lambda_3^2 + \lambda_1^2\lambda_3^2 \\ I_3 &= det[\overline{\boldsymbol{\lambda}}] = \lambda_1^2\lambda_2^2\lambda_3^2 \end{aligned} \tag{52}$$

When a material is incompressible, $\lambda_1\lambda_2\lambda_3 = 1$, regardless of the external tractions. Under these conditions, only two of the stretches are independent. If λ_1 and λ_2 are chosen, then

$$\lambda_3 = \frac{1}{\lambda_1\lambda_2} \tag{53}$$

and the invariants are

$$\begin{aligned} I_1 &= \lambda_1^2 + \lambda_2^2 + \lambda_3^2 \\ I_2 &= \frac{1}{\lambda_1^2} + \frac{1}{\lambda_2^2} + \frac{1}{\lambda_3^2} \\ I_3 &= 1 \end{aligned} \tag{54}$$

Appendix B

Experimental data and Results

p: inflation pressure, r: radius of curvature, λ: stretch ratio, σ: membrane stress

Table B.1
Inflation Test
Pure Gum Rubber

Thickness (t_0): 0.787 mm
Gage length (nom.) l_0: 3 mm
Gage length (meas.) l_0: 2.932 mm
Clamp diam.: 35mm
Gage type: 0-206 kPa (Bourdon)
Supplier: Pacific States Felt
Marking: drafting pen

p	r	λ	σ
kPa	mm	-	MPa
6.89	30.18	1.07	0.150
20.68	22.36	1.18	0.409
27.58	20.12	1.26	0.562
34.47	19.27	1.42	0.846
39.99	17.72	1.81	1.474
41.37	17.96	2.42	2.773
40.68	19.11	2.59	3.320
40.33	18.65	2.72	3.547
39.99	20.00	3.03	4.675
39.30	21.52	3.25	5.679
38.96	20.85	3.52	6.389
38.61	24.59	3.73	8.389
38.27	25.22	3.97	9.673
38.96	30.46	4.31	13.970
39.30	31.39	4.45	15.490

C_{10} = 134.36 kPa
(=1.37 kg/cm^2 = 19.48 psi)
C_{01} = 12.49 kPa
(=0.127 kg/cm^2 = 1.81 psi)

Table B.2
Inflation Test
Natural Latex

Thickness (t_0): 0.762 mm
Gage length (nom.) l_0: 3 mm
Gage length (meas.) l_0: 3.017 mm
Clamp diam.: 35mm
Gage type: 0-206 kPa (Bourdon)
Supplier: McMaster-Carr
Marking: drafting pen

p	r	λ	σ
kPa	mm	-	MPa
6.89	33.37	1.06	0.1705
17.24	23.27	1.14	0.3435
27.58	21.16	1.25	0.5973
34.47	18.72	1.37	0.8005
37.92	18.79	1.50	1.052
39.64	19.04	1.61	1.285
41.02	16.81	1.77	1.418
41.71	17.27	2.02	1.923
41.92	18.54	2.32	2.752
41.37	17.84	2.63	3.345
39.99	19.52	3.01	4.655
38.96	18.84	3.39	5.524
37.92	21.00	3.68	7.085
36.54	22.62	4.00	8.698
36.20	23.42	4.23	9.942
35.85	27.20	4.32	11.94
35.16	25.58	4.59	12.44
34.82	31.11	4.76	16.09
35.16	28.96	4.86	15.76

C_{10} = 181.52 kPa
(=1.85 kg/cm^2 = 26.32 psi)
C_{01} = 6.506 kPa
(=0.066 kg/cm^2 = 0.94 psi)

Table B.3
Inflation Test
Viton™

Thickness (t_0): 0.863 mm
Gage length (nom.) l_0: 6 mm
Gage length (meas.) l_0: 6.084 mm
Clamp diam.: 53.5 mm
Gage type: 0-344 kPa (transducer)
Supplier: McMaster-Carr
Specs: MIL-R-83248 Type 2, Class 1
Marking: silver marker

p	r	λ	σ
kPa	mm	-	MPa
36.24	42.19	1.11	1.091
69.76	33.41	1.23	2.042
105.2	30.17	1.37	3.447
135.7	33.11	1.48	5.695
171.7	30.12	1.63	7.966
198.4	30.68	1.84	11.94
222.9	32.82	2.17	19.90
233.7	33.75	2.48	28.07
222.5	33.49	2.59	29.00

C_{10} = 1194.6 kPa
(=12.18 kg/cm^2 = 173.2 psi)
C_{01} = 163 kPa
(=1.66 kg/cm^2 = 23.64 psi)

Table B.4
Inflation Test
Viton™

Thickness (t_0): 0.838 mm
Gage length (nom.) l_0: 6 mm
Gage length (meas.) l_0: 6.09 mm
Clamp diam.: 53.5 mm
Gage type: 0-344 kPa (transducer)
Supplier: West American Rubber
Specs: MIL-R-83248 Type 2, Class 1
Marking: silver marker

p	r	λ	σ
kPa	mm	-	MPa
35.97	41.95	1.08	1.048
70.38	39.58	1.16	2.223
103.7	32.33	1.24	3.088
138.8	33.7	1.34	5.008
171.	31.9	1.43	6.651
214.2	30.82	1.62	10.37
232.8	30.83	1.75	13.13
247.2	31.88	1.89	16.77
258.5	30.76	2.1	20.83

C_{10} = 1329.2 kPa
(=13.55 kg/cm^2 = 192.7 psi)
C_{01} = 263 kPa
(=2.69 kg/cm^2 = 38.2 psi)

Suppliers:

McMaster-Carr Supply Co., Santa Fe Springs, CA 90670
West American Rubber Co. Inc., Orange, CA 92668
Pacific States Felt & Mfg. Co., Hayward, CA 94545

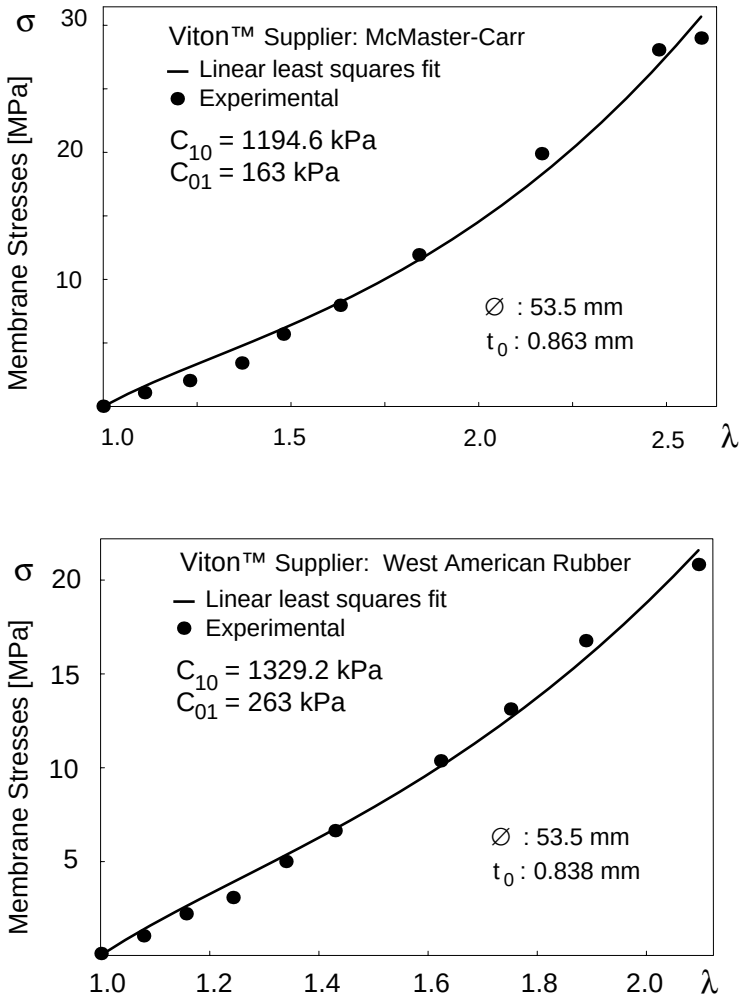

Figure 31: Least squares fit of the experimental data for the tested Viton samples.

Least Squares Fit Example for Pure Gum Rubber

The least squares fit problem expressed by Eq.37 can be set up for a pure gum rubber test by using the fifteen data points listed in Table B.1:

$$\sum_{j=1}^{15} \varphi_1^2(\lambda_j) = 6,704.4$$
$$\sum_{j=1}^{15} \varphi_1(\lambda_j)\varphi_2(\lambda_j) = 102,148$$
$$\sum_{j=1}^{15} \varphi_2^2(\lambda_j) = 1,680,320$$
$$\sum_{j=1}^{15} \varphi_1(\lambda_j)\sigma_j = 2.1773 \times 10^9 Pa$$
$$\sum_{j=1}^{15} \varphi_2(\lambda_j)\sigma_j = 3.4724 \times 10^{10} Pa$$

where

$$\varphi_1(\lambda_j) = 2\left(\lambda_j^2 - \frac{1}{\lambda_j^4}\right)$$
$$\varphi_2(\lambda_j) = 2\left(\lambda_j^4 - \frac{1}{\lambda_j^2}\right)$$

The Mooney-Rivlin coefficients are obtained by solving the following linear system

$$\begin{bmatrix} 6704.4 & 102148 \\ 102148 & 1680320 \end{bmatrix} \begin{Bmatrix} C_{10} \\ C_{01} \end{Bmatrix} = \begin{Bmatrix} 2.1773 \\ 34.724 \end{Bmatrix} \times 10^9 [Pa] \tag{55}$$

i.e.,

$$C_{10} = 134.36 kPa$$
$$C_{01} = 12.49 kPa$$

Appendix C

Sample Abaqus Input File for a Perforated Pad

An Abaqus input file for running a finite element model of a $14\times14\times0.8$mm square pad with a central hole of diameter 4.8mm is shown in the listing on page 48. The numbering scheme for the first layer of nodes is shown in Fig.32, page 52. This input file was generated manually but it could have been obtained with Patran as well. Lines that begin with `*` indicate Abaqus keywords, while those which begin with `**` are comment lines. The rest of the lines are user-defined input values.

The input file is loosely organized into five sections,

- Node definitions.
- Kinematic constraints imposition.
- Element definition.
- Material properties definition.
- Loading imposition and output requests.

No explicit units are indicated in the file, however, all quantities are understood to be expressesd in SI units (dimensions in meters, forces in Newtons, and material constants in Pascals). The results are thus obtained in SI units (stresses in Pascals, displacements in meters).

The analysis has been set up with a $\frac{1}{8}$ model of the actual pad due to symmetry considerations. The lower surface of the pad is compressed against a perfectly rigid surface by a concentrated force acting from above the midsurface of the model. The nodes in the midsurface are constrained to remain on the same $x-y$ plane with a multipoint constraint imposed with `*EQUATION`. A dummy node, numbered 1000, is used to formulate this kinematic constraint. The rigid surface is defined with the `*RIGID SURFACE` keyword which requires additional input to place a local coordinate system and the generator of a plane surface (`START` and `LINE` keywords). It is important that the local coordinate system be defined with its third axis "towards" the 3-D model (the normals of the rigid surfaces and elements in the model must have opposite directions). Otherwise, contact will not be detected. Interface elements associated with the lower rigid surface detect the contact stresses produced by the pad's compression.

A Mooney-Rivlin material with user provided constants is defined with the `*HYPERELASTIC,N=1` option (`N=2` defines a second order deformation form). Perfect friction (infinite friction coefficient) is indicated with `*FRICTION,ROUGH`, while `*SURFACE CONTACT,NO SEPARATION` indicates that once an interface element contacts the rigid surface it remains attached to it for the rest of the analysis.

The *STEP keyword initiates the loading definition and output requests. The *NLGEOM option is turned on to indicate the existence of geometric nonlinearities (large deformations). A maximum number of 400 increments (INCR=400) is allowed in the *STEP line and the imposed load is applied according to a ramp function (AMPLITUDE=RAMP). Ramping the load is a requirement for nonlinear cases where convergence of the solution in a given increment may become very difficult to attain.

A "*RESTART" file is written every 5 increments during the analysis. This file allows the user to restart an analysis or to perform post-processing of the final and intermediate results using Abaqus/Post [40]. The results, stresses, their invariants, and the nodal displacements are also written to binary files using the *NODE FILE and *EL FILE keywords (Patran accepts only this file type for post-processing).

Abaqus Input File Listing

```
**************************************************************
** FINITE ELEMENT MODELING OF A 14x14x0.8MM SQUARE PERFORATED  **
** FLUOROELASTOMER PAD WRL-9/1993                             **
** ABAQUS v.5.2-1                                            **
**************************************************************
*HEADING
PERFORATED VITON PAD D=4.8MM APPLIED FORCE=-19.6N
**DATA CHECK
*********************
** NODE DEFINITION **
*********************
*NODE,NSET=NX1
81,2.4E-3,0,0
101,3E-3,0,0
121,3.65E-3,0,0
141,4.4E-3,0,0
161,5.2E-3,0,0
181,6E-3,0,0
201,7E-3,0,0
99,0,2.4E-3,0
119,0,3E-3,0
139,0,3.65E-3,0
159,0,4.4E-3,0
179,0,5.2E-3,0
199,0,6E-3,0
219,0,7E-3,0
** NODE ASSOCIATED WITH A RIGID SURFACE
*NODE,NSET=RSURFN
1900,0,0,0
*NGEN,LINE=C,NSET=NX2
81,99,1,1900
101,119,1,1900
121,139,1,1900
141,159,1,1900
```

```
161,179,1,1900
181,199,1,1900
201,219,1,1900
*NGEN,LINE=C,NSET=NX2
81,99,1,1900
101,119,1,1900
121,139,1,1900
141,159,1,1900
161,179,1,1900
181,199,1,1900
201,219,1,1900
*NODE,NSET=NX3
202,7E-3,0.6E-3,0
203,7E-3,1.25E-3,0
217,1.25E-3,7E-3,0
218,0.6E-3,7E-3,0
224,7E-3,1.87E-3,0
225,7E-3,2.5E-3,0
226,7E-3,3.25E-3,0
227,7E-3,4.01E-3,0
228,0.00663513,0.00464597,0
229,0.00620496,0.00520658,0
230,0.00572756,0.00572756,0
231,0.00520658,0.00620496,0
232,0.00464597,0.00663513,0
233,4.01E-3,7E-3,0
234,3.25E-3,7E-3,0
235,2.5E-3,7E-3,0
236,1.87E-3,7E-3,0
248,7E-3,4.85E-3,0
249,7E-3,5.8E-3,0
250,6.4E-3,6.4E-3,0
251,5.8E-3,7E-3,0
252,4.85E-3,7E-3,0
270,7E-3,7E-3,0
** DUMMY NODE FOR EQUATION
4000,0,0,0.4E-3
*NCOPY,CHANGE NUMBER=900,OLD SET=NL1,SHIFT,NEW SET=NL4
0,0,0.40E-3
,,,,,,,
*NFILL
NL1,NL4,3,300
*NSET,NSET=XBC,GENERATE
381,501,20
681,801,20
981,1101,20
*NSET,NSET=YBC,GENERATE
399,519,20
699,819,20
```

```
999,1119,20
************************************
** KINEMATIC CONSTRAINT IMPOSITION **
************************************
*EQUATION
2
NL1,3,1,4000,3,-1
*BOUNDARY
XBC,2
YBC,1
RSURFN,1,6
** RIGID SURFACE DEFINITION
*RIGID SURFACE,TYPE=CYLINDER,ELSET=CONTAC
0,0,0,10E-3,0,0
0,10E-3,0
START,0,0
LINE,9E-3,0
************************
** ELEMENT DEFINITION **
************************
*ELEMENT,TYPE=C3D8H
81,81,101,102,82,381,401,402,382
204,204,224,225,205,504,524,525,505
228,228,248,249,229,528,548,549,529
*ELEMENT,TYPE=C3D6H
203,203,224,204,503,524,504
250,250,270,251,550,570,551
*ELGEN,ELSET=EL1
81,18,1,1,6,20,20,3,300,300
204,12,1,1,3,300,300
228,4,1,1,3,300,300
203,2,24,24,3,300,300
227,2,22,22,3,300,300
250,2,-18,-18,3,300,300
232,2,-16,-16,3,300,300
** INTERFACE ELEMENT DEFINITION (DETECTION OF
** CONTACT WITH RIGID SURFACE)
*ELEMENT,TYPE=IRS4
** LOWER PAD SURFACE 2081,81,101,102,82,1900
2204,204,224,225,205,1900
2228,228,248,249,229,1900
** LATERAL,HOLE
3081,81,381,382,82,1900
** LATERAL,EDGE
3201,201,202,502,501,1900
3203,203,224,524,503,1900
3224,224,225,525,524,1900
3218,219,519,518,218,1900
3236,217,517,536,236,1900
3235,236,536,535,235,1900
*ELEMENT,TYPE=IRS3
```

```
2203,203,224,204,1900
2250,250,270,251,1900
*ELGEN,ELSET=CONTAC
** LOWER PAD SURFACE
2081,18,1,1,6,20,20
2204,12,1,1
2228,4,1,1
2203,2,24,24
2227,2,22,22
2250,2,-18,-18
2232,2,-16,-16
** LATERAL,HOLE
3081,18,1,1,2,300,30
** LATERAL,EDGE
3201,2,1,1,2,300,300
3203,2,24,24,2,300,300
3224,3,1,1,2,300,300
3226,2,22,22,2,300,300
3227,2,22,22,2,300,300
3218,2,-1,-1,2,300,300
3236,2,16,16,2,300,300
3235,3,-1,-1,2,300,300
3233,2,18,18,2,300,300
3252,2,18,18,2,300,300
**********************************************
** MATERIAL PROPERTIES DEFINITION, MOONEY-RIVLIN **
** HYPERELASTIC C10=1.194MPa C01=0.163MPa        **
**********************************************
*MATERIAL,NAME=VITON
*HYPERELASTIC,N=1
1.194E6,0.163E6
*SOLID SECTION,ELSET=EL1,MATERIAL=VITON
*INTERFACE,ELSET=CONTAC
*FRICTION,ROUGH
*SURFACE CONTACT,NO SEPARATION
**********************************
** LOADING AND OUTPUT DEFINITION **
**********************************
*RESTART,WRITE,FREQUENCY=5
*STEP,NLGEOM,INC=400,AMPLITUDE=RAMP
*STATIC
0.1,1,1E-20,0.1
*CLOAD
1049,3,-19.6
*PRINT,CONTACT=YES
*EL PRINT,ELSET=EL1,POSITION=AVERAGED AT NODES,FREQUENCY=5
S,MISES
E
*EL PRINT,ELSET=CONTAC,POSITION=AVERAGED AT NODES,FREQUENCY=5
S
*NODE PRINT,FREQUENCY=5
```

```
U
*NODE FILE
COORD
U
*EL FILE
S,SINV
*END STEP
```

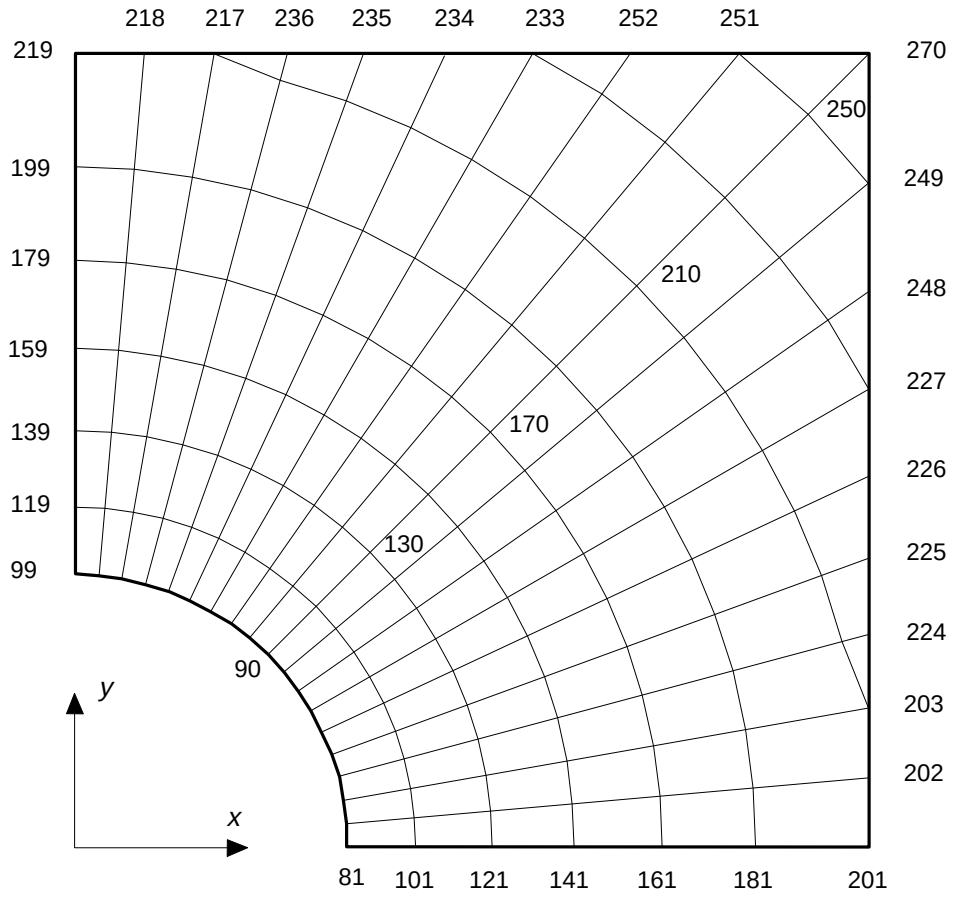

Figure 32: Numbering scheme for the first layer of nodes (z=0).

References

[1] Hamburgen, W., Fitch, J.S., "Packaging a 150-W Bipolar ECL Microprocessor," IEEE Trans.CHMT, Vol.16, No.1, pp 28-38 (Feb 1993)

[2] Wessely, H., Türk, W., Schmidt, K.H., Nagel, G., "Computer Packaging," Siemens Forsch.-u. Entwickl.-Ber., Vol.17, No.5, pp.234-239 (1988)

[3] Wessely, H., "Packaging System for High Performance Computer," Proc.Sixth IEEE/ CHMT Int.Electronic Manufacturing Technology Symposium, Nara, Japan, Apr.26-28, 1989, pp.83-89, IEEE, NJ (1989)

[4] Hacke, H.-J., private communication (Oct.1993).

[5] Du Pont Polymers Inc., "Viton Selection Guide," Cat.# 226965B, Wilmington, DE 19880-0011 (1992)

[6] Arnold, R.G., Barney, A.L., Thompson, D.C., "Fluoroelastomers," Rubber Chem.Tech- nol., Vol.46, No.3, pp.619-651 (1973)

[7] Treloar, L.R.G., "The Physics of Rubber Elasticity," Clarendon Press, Oxford (1958)

[8] Malvern, L.W., "Introduction to the Mechanics of a Continuum Medium," Prentice-Hall, Englewood Cliffs, N.J. (1969)

[9] Green, A.E., Adkins, J.E., "Large Elastic Deformations," Clarendon Press, Oxford, (1970)

[10] Green, A.E., Zerna, W., "Theoretical Elasticity," Clarendon Press, Oxford (1968)

[11] Oden, J.T., "Finite Elements of Nonlinear Continua," McGraw-Hill, New York (1972)

[12] Rivlin, R.S., "Large Elastic Deformations of Isotropic Materials IV. Further Developments of the General Theory," Phil.Trans.Roy.Soc., Vol.A241, No.835, pp.379-397 (Oct.5,1948)

[13] Mooney, M., "A Theory of Large Elastic Deformation," J.Appl.Phys, Vol.11, No.9, pp.582-592 (Sep.1940)

[14] Rivlin, R.S., Saunders, D.W., "Large Elastic Deformations of Isotropic Materials VII. Experiments on the Deformation of Rubber," Phil.Trans.Roy.Soc., Vol.A243, No.865, pp.251-288 (Apr.24,1951)

[15] Klosner, J.M., Segal, A., "Mechanical Characterization of a Natural Rubber," PIBAL Report No.69-42, Dept.of Aerospace Engineering and Applied Mechanics, Polytechnic Institute of Brooklyn (Oct.1969)

[16] Ishihara, A., Hashitsume, N., Tatibana, M., "Statistical Theory of Rubber-Like Elasticity IV (Two-Dimensional Stretching)," J.Chem.Phys., Vol.19, No.12, pp.1508-1512 (Dec.1951)

[17] Alexander, H., "A Constitutive Relation for Rubber-Like Materials," Int.J.Engng.Sci., Vol.6, No.9, pp.549-563 (Sep.1968) [Oden '72 p.388]

[18] James, A.G., Green, A., Simpson, G.M., "Strain Energy Functions of Rubber I. Characterization of Gum Vulcanizates," J.Appl.Polymer Sci., Vol.19, No.3, pp.2033-2058 (Mar.1975)

[19] Morman, K.N., Pan, T.Y., "Application of Finite-Element Analysis in the Design of Automotive Elastomeric Components," Rubber Chem.Technol., Vol.61, No.3, pp.503-533 (Jul.-Aug.1988)

[20] Yeoh, O.H., "Characterization of Elastic Properties of Carbon-Black-Filled Rubber Vulcanizates," Rubber Chem.Technol., Vol.63, No.5, pp.792-805 (Nov.-Dec.,1990)

[21] Hart-Smith, L.J., "Elasticity Parameters for Finite Deformations of Rubber-like Materials," Z.angew.Math.Phys., Vol.17, No.5, pp.608-626 (Sep.1966)

[22] Hart-Smith, L.J., Crisp, J.D.C., "Large Elastic Deformations of Thin Rubber Membranes," Int.J.Eng.Sci., Vol.5, No.1, pp.1-24 (1967)

[23] Ogden, R.W., "Large Deformation Isotropic Elasticity - On the Correlation of Theory and Experiment for Incompressible Rubberlike Solids," Proc.Roy.Soc.Lond., Vol.A326, No.1567, pp.565-584 (Feb.1972)

[24] Hall, M.M,"Pressure Distribution over the Flat End Surfaces of Compressed Solid-Rubber Cylinders, J.Strain Analysis, Vol.6, No.1, pp.38-44, (Jan.1971)

[25] Treloar, L.R.G., "Stresses and Birefringence in Rubber Subjected to General Homogeneous Strain," Proc.Phys.Soc., Vol.60 pt.2, No.338, pp.135-144 (Feb.1,1948)

[26] Treloar, L.R.G., "Stress-Strain Data for Vulcanised Rubber under Various Types of Deformation," Trans.Faraday Soc., Vol.40, pp.59-70 (1944)

[27] Treloar, L.R.G., "Strains in an Inflated Rubber Sheet, and the Mechanism of Bursting," Trans.I.R.I., Vol.19, pp.201-212 (1944)

[28] Adkins, J.E., Rivlin, R.S., "Large Elastic Deformation of Isotropic Materials IX. The Deformation of Thin Shells," Phil.Trans.Roy.Soc., Vol.A244, No.888, pp.66-531 (May 7, 1952)

[29] Oden, J.T., Kubitza, W.K., "Numerical Analysis of Nonlinear Pneumatic Structures," Proc. 1st Int. Colloquium on Pneumatic Structures, Stuttgart, May 11-12, 1967, pp.87-107, Technische Hochschule, Stuttgart (1967)

[30] Finney, R.H., Kumar, A., "Development of Material Constants for Nonlinear Finite-Element Analysis," Rubber Chem.Technol., Vol.61, No.5, pp.879-891 (Nov-Dec.1988)

[31] Kong, D., White, J.L., "Inflation Characteristics of Unvulcanized Gum and Compounded Rubber Sheets," Rubber Chem.Technol., Vol.59, No.2, pp.315-327 (May-Jun.1986)

[32] ASTM D412-92, "Standard Test Methods for Vulcanized Rubber and Thermoplastic Rubbers and Thermoplastic Elastomers - Tension," Annual Book of ASTM Standards, Section 9, Vol.09.01, Rubber, Natural and Synthetic - General Test Methods; Carbon Black, American Society for Testing and Materials, Philadelphia (1993)

[33] Alexander, H., "Tensile Instability of Initially Spherical Balloons," Int.J.Engng.Sci., Vol.9, No.1, pp.151-162 (Jan.1971)

[34] Needleman, A., "Inflation of Spherical Rubber Balloons," Int.J.Solids Struct., Vol.13, No.5, pp.409-421 (1977)

[35] Twizell, E.H., Ogden, R.W., "Non-linear Optimization of the Material Constants in Ogden's Stress-Deformation Function for Incompressible Isotropic Elastic Materials," J.Austral.Math.Soc., Ser.B., Vol.24, pp.424-434 (1983)

[36] Atkinson, K.E., "Elementary Numerical Analysis," J.Wiley & Sons, New York (1985)

[37] Hibbit, Karlsson, & Sorensen, Inc., “Abaqus/Standard User’s Manual v.5.2,” Vol.I & II, HKS, Pawtucket, RI (1992)

[38] PDA Engineering, “P3/PATRAN User Manual,” Costa Mesa, CA (1993)

[39] Mase, G.E., Mase, G.T., “Continuum Mechanics for Engineers,” CRC Press, Boca Raton, FL (1992)

[40] Hibbit, Karlsson, & Sorensen, Inc., “Abaqus/Post User’s Manual v.5.2,” HKS, Pawtucket, RI (1992)

WRL Research Reports

‘‘Titan System Manual.’’
Michael J. K. Nielsen.
WRL Research Report 86/1, September 1986.

‘‘Global Register Allocation at Link Time.’’
David W. Wall.
WRL Research Report 86/3, October 1986.

‘‘Optimal Finned Heat Sinks.’’
William R. Hamburgen.
WRL Research Report 86/4, October 1986.

‘‘The Mahler Experience: Using an Intermediate Language as the Machine Description.’’
David W. Wall and Michael L. Powell.
WRL Research Report 87/1, August 1987.

‘‘The Packet Filter: An Efficient Mechanism for User-level Network Code.’’
Jeffrey C. Mogul, Richard F. Rashid, Michael J. Accetta.
WRL Research Report 87/2, November 1987.

‘‘Fragmentation Considered Harmful.’’
Christopher A. Kent, Jeffrey C. Mogul.
WRL Research Report 87/3, December 1987.

‘‘Cache Coherence in Distributed Systems.’’
Christopher A. Kent.
WRL Research Report 87/4, December 1987.

‘‘Register Windows vs. Register Allocation.’’
David W. Wall.
WRL Research Report 87/5, December 1987.

‘‘Editing Graphical Objects Using Procedural Representations.’’
Paul J. Asente.
WRL Research Report 87/6, November 1987.

‘‘The USENET Cookbook: an Experiment in Electronic Publication.’’
Brian K. Reid.
WRL Research Report 87/7, December 1987.

‘‘MultiTitan: Four Architecture Papers.’’
Norman P. Jouppi, Jeremy Dion, David Boggs, Michael J. K. Nielsen.
WRL Research Report 87/8, April 1988.

‘‘Fast Printed Circuit Board Routing.’’
Jeremy Dion.
WRL Research Report 88/1, March 1988.

‘‘Compacting Garbage Collection with Ambiguous Roots.’’
Joel F. Bartlett.
WRL Research Report 88/2, February 1988.

‘‘The Experimental Literature of The Internet: An Annotated Bibliography.’’
Jeffrey C. Mogul.
WRL Research Report 88/3, August 1988.

‘‘Measured Capacity of an Ethernet: Myths and Reality.’’
David R. Boggs, Jeffrey C. Mogul, Christopher A. Kent.
WRL Research Report 88/4, September 1988.

‘‘Visa Protocols for Controlling Inter-Organizational Datagram Flow: Extended Description.’’
Deborah Estrin, Jeffrey C. Mogul, Gene Tsudik, Kamaljit Anand.
WRL Research Report 88/5, December 1988.

‘‘SCHEME->C A Portable Scheme-to-C Compiler.’’
Joel F. Bartlett.
WRL Research Report 89/1, January 1989.

‘‘Optimal Group Distribution in Carry-Skip Adders.’’
Silvio Turrini.
WRL Research Report 89/2, February 1989.

‘‘Precise Robotic Paste Dot Dispensing.’’
William R. Hamburgen.
WRL Research Report 89/3, February 1989.

''Simple and Flexible Datagram Access Controls for Unix-based Gateways.''
Jeffrey C. Mogul.
WRL Research Report 89/4, March 1989.

''Spritely NFS: Implementation and Performance of Cache-Consistency Protocols.''
V. Srinivasan and Jeffrey C. Mogul.
WRL Research Report 89/5, May 1989.

''Available Instruction-Level Parallelism for Superscalar and Superpipelined Machines.''
Norman P. Jouppi and David W. Wall.
WRL Research Report 89/7, July 1989.

''A Unified Vector/Scalar Floating-Point Architecture.''
Norman P. Jouppi, Jonathan Bertoni, and David W. Wall.
WRL Research Report 89/8, July 1989.

''Architectural and Organizational Tradeoffs in the Design of the MultiTitan CPU.''
Norman P. Jouppi.
WRL Research Report 89/9, July 1989.

''Integration and Packaging Plateaus of Processor Performance.''
Norman P. Jouppi.
WRL Research Report 89/10, July 1989.

''A 20-MIPS Sustained 32-bit CMOS Microprocessor with High Ratio of Sustained to Peak Performance.''
Norman P. Jouppi and Jeffrey Y. F. Tang.
WRL Research Report 89/11, July 1989.

''The Distribution of Instruction-Level and Machine Parallelism and Its Effect on Performance.''
Norman P. Jouppi.
WRL Research Report 89/13, July 1989.

''Long Address Traces from RISC Machines: Generation and Analysis.''
Anita Borg, R.E.Kessler, Georgia Lazana, and David W. Wall.
WRL Research Report 89/14, September 1989.

''Link-Time Code Modification.''
David W. Wall.
WRL Research Report 89/17, September 1989.

''Noise Issues in the ECL Circuit Family.''
Jeffrey Y.F. Tang and J. Leon Yang.
WRL Research Report 90/1, January 1990.

''Efficient Generation of Test Patterns Using Boolean Satisfiablilty.''
Tracy Larrabee.
WRL Research Report 90/2, February 1990.

''Two Papers on Test Pattern Generation.''
Tracy Larrabee.
WRL Research Report 90/3, March 1990.

''Virtual Memory vs. The File System.''
Michael N. Nelson.
WRL Research Report 90/4, March 1990.

''Efficient Use of Workstations for Passive Monitoring of Local Area Networks.''
Jeffrey C. Mogul.
WRL Research Report 90/5, July 1990.

''A One-Dimensional Thermal Model for the VAX 9000 Multi Chip Units.''
John S. Fitch.
WRL Research Report 90/6, July 1990.

''1990 DECWRL/Livermore Magic Release.''
Robert N. Mayo, Michael H. Arnold, Walter S. Scott, Don Stark, Gordon T. Hamachi.
WRL Research Report 90/7, September 1990.

''Pool Boiling Enhancement Techniques for Water at Low Pressure.''
Wade R. McGillis, John S. Fitch, William R. Hamburgen, Van P. Carey.
WRL Research Report 90/9, December 1990.

''Writing Fast X Servers for Dumb Color Frame Buffers.''
Joel McCormack.
WRL Research Report 91/1, February 1991.

''A Simulation Based Study of TLB Performance.''
J. Bradley Chen, Anita Borg, Norman P. Jouppi.
WRL Research Report 91/2, November 1991.

''Analysis of Power Supply Networks in VLSI Circuits.''
Don Stark.
WRL Research Report 91/3, April 1991.

''TurboChannel T1 Adapter.''
David Boggs.
WRL Research Report 91/4, April 1991.

''Procedure Merging with Instruction Caches.''
Scott McFarling.
WRL Research Report 91/5, March 1991.

''Don't Fidget with Widgets, Draw!.''
Joel Bartlett.
WRL Research Report 91/6, May 1991.

''Pool Boiling on Small Heat Dissipating Elements in Water at Subatmospheric Pressure.''
Wade R. McGillis, John S. Fitch, William R. Hamburgen, Van P. Carey.
WRL Research Report 91/7, June 1991.

''Incremental, Generational Mostly-Copying Garbage Collection in Uncooperative Environments.''
G. May Yip.
WRL Research Report 91/8, June 1991.

''Interleaved Fin Thermal Connectors for Multichip Modules.''
William R. Hamburgen.
WRL Research Report 91/9, August 1991.

''Experience with a Software-defined Machine Architecture.''
David W. Wall.
WRL Research Report 91/10, August 1991.

''Network Locality at the Scale of Processes.''
Jeffrey C. Mogul.
WRL Research Report 91/11, November 1991.

''Cache Write Policies and Performance.''
Norman P. Jouppi.
WRL Research Report 91/12, December 1991.

''Packaging a 150 W Bipolar ECL Microprocessor.''
William R. Hamburgen, John S. Fitch.
WRL Research Report 92/1, March 1992.

''Observing TCP Dynamics in Real Networks.''
Jeffrey C. Mogul.
WRL Research Report 92/2, April 1992.

''Systems for Late Code Modification.''
David W. Wall.
WRL Research Report 92/3, May 1992.

''Piecewise Linear Models for Switch-Level Simulation.''
Russell Kao.
WRL Research Report 92/5, September 1992.

''A Practical System for Intermodule Code Optimization at Link-Time.''
Amitabh Srivastava and David W. Wall.
WRL Research Report 92/6, December 1992.

''A Smart Frame Buffer.''
Joel McCormack & Bob McNamara.
WRL Research Report 93/1, January 1993.

''Recovery in Spritely NFS.''
Jeffrey C. Mogul.
WRL Research Report 93/2, June 1993.

''Tradeoffs in Two-Level On-Chip Caching.''
Norman P. Jouppi & Steven J.E. Wilton.
WRL Research Report 93/3, October 1993.

''Unreachable Procedures in Object-oriented Programing.''
Amitabh Srivastava.
WRL Research Report 93/4, August 1993.

''Limits of Instruction-Level Parallelism.''
David W. Wall.
WRL Research Report 93/6, November 1993.

‘‘Fluoroelastomer Pressure Pad Design for Microelectronic Applications.’’
Alberto Makino, William R. Hamburgen, John S. Fitch.
WRL Research Report 93/7, November 1993.

WRL Technical Notes

‘‘TCP/IP PrintServer: Print Server Protocol.’’
Brian K. Reid and Christopher A. Kent.
WRL Technical Note TN-4, September 1988.

‘‘TCP/IP PrintServer: Server Architecture and Implementation.’’
Christopher A. Kent.
WRL Technical Note TN-7, November 1988.

‘‘Smart Code, Stupid Memory: A Fast X Server for a Dumb Color Frame Buffer.’’
Joel McCormack.
WRL Technical Note TN-9, September 1989.

‘‘Why Aren’t Operating Systems Getting Faster As Fast As Hardware?’’
John Ousterhout.
WRL Technical Note TN-11, October 1989.

‘‘Mostly-Copying Garbage Collection Picks Up Generations and C++.’’
Joel F. Bartlett.
WRL Technical Note TN-12, October 1989.

‘‘The Effect of Context Switches on Cache Performance.’’
Jeffrey C. Mogul and Anita Borg.
WRL Technical Note TN-16, December 1990.

‘‘MTOOL: A Method For Detecting Memory Bottlenecks.’’
Aaron Goldberg and John Hennessy.
WRL Technical Note TN-17, December 1990.

‘‘Predicting Program Behavior Using Real or Estimated Profiles.’’
David W. Wall.
WRL Technical Note TN-18, December 1990.

‘‘Cache Replacement with Dynamic Exclusion’’
Scott McFarling.
WRL Technical Note TN-22, November 1991.

‘‘Boiling Binary Mixtures at Subatmospheric Pressures’’
Wade R. McGillis, John S. Fitch, William R. Hamburgen, Van P. Carey.
WRL Technical Note TN-23, January 1992.

‘‘A Comparison of Acoustic and Infrared Inspection Techniques for Die Attach’’
John S. Fitch.
WRL Technical Note TN-24, January 1992.

‘‘TurboChannel Versatec Adapter’’
David Boggs.
WRL Technical Note TN-26, January 1992.

‘‘A Recovery Protocol For Spritely NFS’’
Jeffrey C. Mogul.
WRL Technical Note TN-27, April 1992.

‘‘Electrical Evaluation Of The BIPS-0 Package’’
Patrick D. Boyle.
WRL Technical Note TN-29, July 1992.

‘‘Transparent Controls for Interactive Graphics’’
Joel F. Bartlett.
WRL Technical Note TN-30, July 1992.

‘‘Design Tools for BIPS-0’’
Jeremy Dion & Louis Monier.
WRL Technical Note TN-32, December 1992.

‘‘Link-Time Optimization of Address Calculation on a 64-Bit Architecture’’
Amitabh Srivastava and David W. Wall.
WRL Technical Note TN-35, June 1993.

‘‘Combining Branch Predictors’’
Scott McFarling.
WRL Technical Note TN-36, June 1993.

‘‘Boolean Matching for Full-Custom ECL Gates’’
Robert N. Mayo and Herve Touati.
WRL Technical Note TN-37, June 1993.